frontiers in Earth Science

ORIGINAL RESEARCH
published: 01 July 2021
doi: 10.3389/feart.2021.683312

Gem-Grade Garnet With Metamorphic Origin in the Tiemurt Orogenic-Type Deposit, Chinese Altay Orogen: Texture, Chemistry, and Physicochemical Condition

Zhaobin Hu[1], *Yi Zheng*[1,2,3]*, *Pengpeng Yu*[1,2], *Yihan Wu*[1] *and Chengming Wang*[1,3]

[1]Guangdong Provincial Key Lab of Geological Process and Mineral Resources Survey, School of Earth Sciences and Geological Engineering, Sun Yat-Sen University, Guangzhou, China, *[2]Guangdong Provincial Key Lab of Geodynamic and Geohazards, Sun Yat-Sen University, Guangzhou, China,* *[3]Southern Marine Science and Engineering Guangdong Laboratory, Zhuhai, China*

The Chinese Altay Orogen represents an accretionary collage with episodic subduction-related accretion from the Neoproterozoic to Permian, followed by Triassic continent–continent collision. Reddish gem-grade garnet grains are widespread in Au–Cu–Pb–Zn sulfide deposits of the Chinese Altay Orogen, and how their formation links to regional geological processes such as seafloor sedimentation, magmatic hydrothermal metasomatic, or orogenic metamorphism remains unclear. In this context, we present an integrated set of geological occurrences, mineral texture, and major trace elemental geochemistry of six garnet grains from the representative Tiemurt Cu–Pb–Zn(-Au) deposit. Two categories of garnets, Grt1 and Grt2, are identified in terms of distinct mineral assemblages, textures, and geochemistry. The sub- to euhedral biotite inclusion–rich Grt1 with fine grains of less than 0.3 cm in diameter is intergrown with amphibole, chlorite, and biotite. Comparatively, the euhedral mineral inclusion–poor Grt2 with coarse grains of 0.5–5 cm in diameter is paragenetic with quartz, calcite, chlorite, and biotite. Forty-one EMPA analyses show that Grt1 and Grt2 have similar major elemental compositions of SiO_2 (36.2–37.5 wt%), Al_2O_3 (19.9–20.7 wt%), and CaO (5.3–7.8 wt%) but host variable contents of FeO (31.7–35.9 wt% for Grt1 and 23.0–30.0 wt % for Grt2) and MnO (0.8–3.7 wt% for Grt1 and 4.3–12.7 wt% for Grt2). Both Grt1 (with a chemical formula of $Alm_{49.3–54.6}Spe_{19.7–24.6}Gro_{14.6–18.4}Pyr_{3.7–4.8}And_{3.5–4.9}$) and Grt2 ($Alm_{57.4–64.4}Gro_{15.5–18.3}Spe_{9.62–19.8}Pyr_{3.8–5.7}And_{1.1–4.4}$) are plotted into the field close to the end-member of almandine (Fe-Al–garnet). Compared to Grt1, Grt2 displays a Fe-enriched and Mn-depleted trend. Additionally, Mn is enriched in the core but Fe is enriched in the rim on the major elemental profile of Grt1. Regarding the trends of trace elements and REEs, Grt2 is believed to be produced during the detriment and replacement of Grt1 by an intense external metal-rich fluid. In combination with previous fluid inclusion research, the garnet-related fluids are characterized by CO_2-rich, mesothermal, mildly acidic, and reduced redox, analogous to metamorphic fluids generated during orogenesis. Collectively, we conclude that the reddish gem-grade garnet crystals in the Chinese Altay Orogen are of metamorphic origin.

Keywords: garnet, metamorphic origin, orogenic-type deposit, Tiemurt Pb–Zn–Cu deposit, Chinese Altay Orogen

Edited by:
Xiaohua Deng,
Beijing Institute of Geology for Mineral Resources, China

Reviewed by:
Yu Zhang,
Central South University, China
Pei Liang,
University of Science and Technology Beijing, China

****Correspondence:***
Yi Zheng
zhengy43@mail.sysu.edu.cn

Specialty section:
This article was submitted to Economic Geology, a section of the journal Frontiers in Earth Science

Received: *20 March 2021*
Accepted: *07 June 2021*
Published: *01 July 2021*

Citation:
Hu Z, Zheng Y, Yu P, Wu Y and Wang C (2021) Gem-Grade Garnet With Metamorphic Origin in the Tiemurt Orogenic-Type Deposit, Chinese Altay Orogen: Texture, Chemistry, and Physicochemical Condition. Front. Earth Sci. 9:683312. doi: 10.3389/feart.2021.683312

INTRODUCTION

Garnet is a widespread silicate mineral in variable geological settings on Earth, for example, mantle transition zone, subducting ocean crust, skarn deposits with magmatic hydrothermal origin, seafloor sedimentary exhalation, and metamorphic rocks (Marco and Donald, 1982; Doyle and Allen, 2003; Meinert et al., 2005). Different garnets host a similar crystal structure of [SiO_4] tetrahedrons with the chemical formula of $A_3B_2(SiO_4)_3$, in which A = Ca^{2+}, Fe^{2+}, Mg^{2+}, and/or Mn^{2+}, while B = Al^{3+}, Fe^{3+}, and/or Cr^{3+} (Menzer, 1926; Bernard et al., 2013; Dietrich, 2020). Two principal categories of garnets with different chemical compositions have been well documented, that is, the Al-rich garnet (represented by pyrope, almandine, and spessartine) and Fe-rich garnet (grossular, uvarovite, and andradite) (Charles, 2016). In particular, the chemical variations of these garnets, coupled with mineral growth zonation, are often used as a sensitive indicator of physicochemical conditions, such as pressure (P), temperature (T), redox state, and acidity (Jamtveit et al., 1993; Konrad-Schmolke et al., 2005; Baxter and Scherer, 2013). Linkage of garnet mineral growth and metal accumulation has received much attention in the skarn deposits (Jamtveit et al., 1993), owing to the substantial Ca-rich garnet produced by contact replacement of magmatic fluids with host carbonates (Xu et al., 2016; Park et al., 2019). However, garnet geological indicator is rarely used in other genetic-type metal deposits largely because of its scarcity.

An abundance of reddish gem-grade garnet has been discovered in the Au–Cu–Pb–Zn polymetallic ore deposits in the Chinese Altay Orogen, but their origin remains unclear (Chen, 2000; Yang et al., 2018). In fact, ore genesis of these polymetallic ore deposits is also intensively debated as the volcanogenetic massive sulfide (VMS), metamorphosed VMS, or orogeny-driven metamorphic hydrothermal (orogenic-type) deposits (Zheng et al., 2013b; Stefanie et al., 2014). These controversies are partially due to most of these polymetallic deposits possessing significant characteristics of textural modification and chemical remobilization during the subsequently magmatic and metamorphic overprinting (Jamtveit et al., 1993; Ciobanu and Cook, 2004; Barrie et al., 2010). It is hard to evaluate the contribution of seafloor sedimentation or subsequent orogenesis for these polymetallic deposits in the Chinese Altay Orogen (Yu and Zheng, 2019). Therefore, these garnet grains have great potential to answer the questions of how the metals were enriched up to ores.

The representative Tiemurt Pb–Zn–(Cu–Au) deposit hosts large amounts of garnet grains paragenetic with the chief sulfide ores (Zheng et al., 2013a; Zhang et al., 2017a; Yu and Zheng, 2019). To address the above scientific issue, we conducted an integrated set of paragenetic sequence, internal textures, and their corresponding *in situ* major and minor elemental compositions of the Tiemurt garnet. The growth history and physicochemical condition of garnet is believed to assist to yield much clearer understanding on the ore genesis and regional metallogeny (Konrad-Schmolke et al., 2005). In addition, this research might shed light on the reconstruction of tectonic evolution of the Chinese Altay Orogen and even CAOB.

GEOLOGICAL BACKGROUND

Tectonic Settings

The Central Asian Orogenic Belt (CAOB), the largest accretionary orogen on Earth (Jahn, 2004; Xiao et al., 2009; Chen et al., 2012), is located between the Siberia Craton to the north and Tarim-Sinokorea Craton to the south (**Figure 1A**). An abundance of Paleozoic ophiolites, arc igneous rocks, and Precambrian massifs records a complex accretionary history prior to the Triassic collisions of the Siberian with Tarim-Sinokorea Craton (Xiao et al., 2009).

As an important element of CAOB, the Chinese Altay Orogen is an accretionary complexity toward the southern margin of the Siberian Craton and contains four principle tectonic units from north to south (**Figure 1B**; Chen et al., 2012), including 1) Unit 1: the Late Devonian–Early Carboniferous Nurt volcanic basin developed on a Precambrian crystalline basement; 2) Unit 2: the Paleozoic Keketuohai magmatic arc that contains Precambrian high-grade metamorphic rocks, Neoproterozoic–Earliest Triassic granites, and the giant Keketuohai pegmatite field; 3) Unit 3: the Devonian–Carboniferous volcanic basins developed on the southern margin of the pre-Devonian metamorphic rocks, for example, the Kelan, Ashele, and Maizi basins; and 4) Unit 4: the Armantay–Ertix accretionary terrane and Devonian–Carboniferous fossiliferous sedimentary rocks, intruded by post-orogenic granites.

The basins in Unit 3 of the Chinese Altay Orogen is filled by a package of low-grade metamorphosed volcano-sedimentary rocks comprising the continentally derived turbidites (e.g., Habahe Group), volcanic rocks (e.g., Altay Formation), and volcanic-sedimentary rocks (e.g., Kangbutiebao Formation) (Wang et al., 1998; Goldfarb et al., 2003). It is notable that these basins are metal-fertile and hosting considerable amount of metal deposits. The representative deposits include the giant Ashele Cu–Zn, Keketale Pb–Zn, Mengku Fe deposits (Wang et al., 1998; Wan et al., 2010a, 2010b; Zheng et al., 2013b), and numerous polymetallic lode deposits (**Figure 2A**; e.g., the Sarekuobu Au, the Wulasigou Cu deposit, and Tiemurt Au–Cu–Pb–Zn deposits (Zhang et al., 2012; Zheng et al., 2012; Yu et al., 2020).

Field Geology of the Kelan Basin

The Kelan Basin is particularly rich in the Au–Cu–Pb–Zn lode deposits that are controlled by a series of complex structures. A huge multiple overturned syncline system, with the axial plane dipping toward northwest, is identified in the Kelan Basin (**Figure 2A**). The well-developed NW-trending faults are the chief ore-controlled structures and also separate the distinct stratigraphic units, that is, the Keyingong and Hongdun faults separate the Kulumuti Group and the Kangbutiebao Formation, while the Abagong and Altay faults separate the Kangbutiebao and Altay Formations (**Figure 2A**).

Among the strata, the Silurian Kulumiti Group with lithological composition of migmatite, gneiss, and schist is unconformably overlain by the Devonian Kangbutiebao and Altay formations. The Kangbutiebao Formation consists of a set of felsic lavas, pyroclastic rocks, and siliciclastic

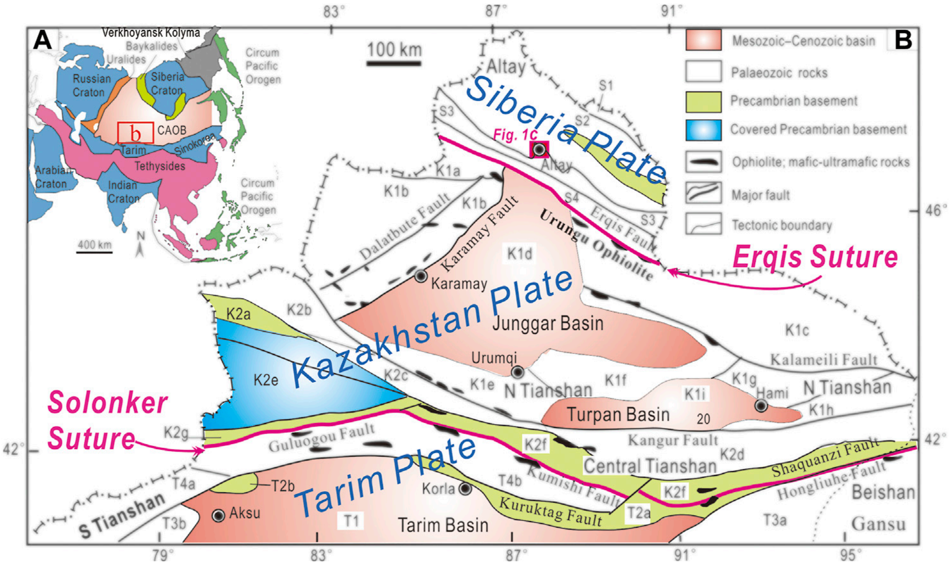

FIGURE 1 | (A) Tectonic framework of the Central Asian Orogenic Belt. **(B)** Geological sketch map showing the tectonic units of North Xinjiang (Chen et al., 2012). Siberia plate: S1, Late Devonian–Early Carboniferous Nurt volcanic basin; S2, Paleozoic Keketuohai magmatic arc; S3, Devonian–Carboniferous Kelan forearc basin; S4, Armantay-Irtysh accretionary wedge. Kazakhstan plate; K1a, Zharma-Sawur island arc; K1b, Western Junggar accretionary complex; K1c, Eastern Junggar accretionary complex; K1d, Mesozoic–Cenozoic Junggar basin; K1e, Late Paleozoic Yelianhabirga backarc basin; K1f, Late Paleozoic Bogada aulacogen; K1g, Paleozoic Harlike island arc; K1h, Dananhu island arc; K1i, Mesozoic–Cenozoic Turpan basin; K2a, Sailimu massif; K2b, Wenquan terrane; K2c, Paleozoic Boloholo arc basin system; K2d, Paleozoic Yamansu-Jueluotag arc basin system; K2e, Carboniferous–Permian Ili rift; K2f, Early Paleozoic central Tianshan island arc with Precambrian fragments; K2g, Nalati massif. Tarim Plate: T1, Mesozoic–Cenozoic Tarim basin; T2a, Precambrian Kuruktag massif; T2b, Muzart massif; T3a, Carboniferous–Permian Beishan aulacogen; T3b, Late Paleozoic Kalatierek passive marginal sediments; T4a, Late Paleozoic Southwest Tianshan fold-thrust belt; T4b, Paleozoic Southern Tianshan (or Kumishi) accretionary complex.

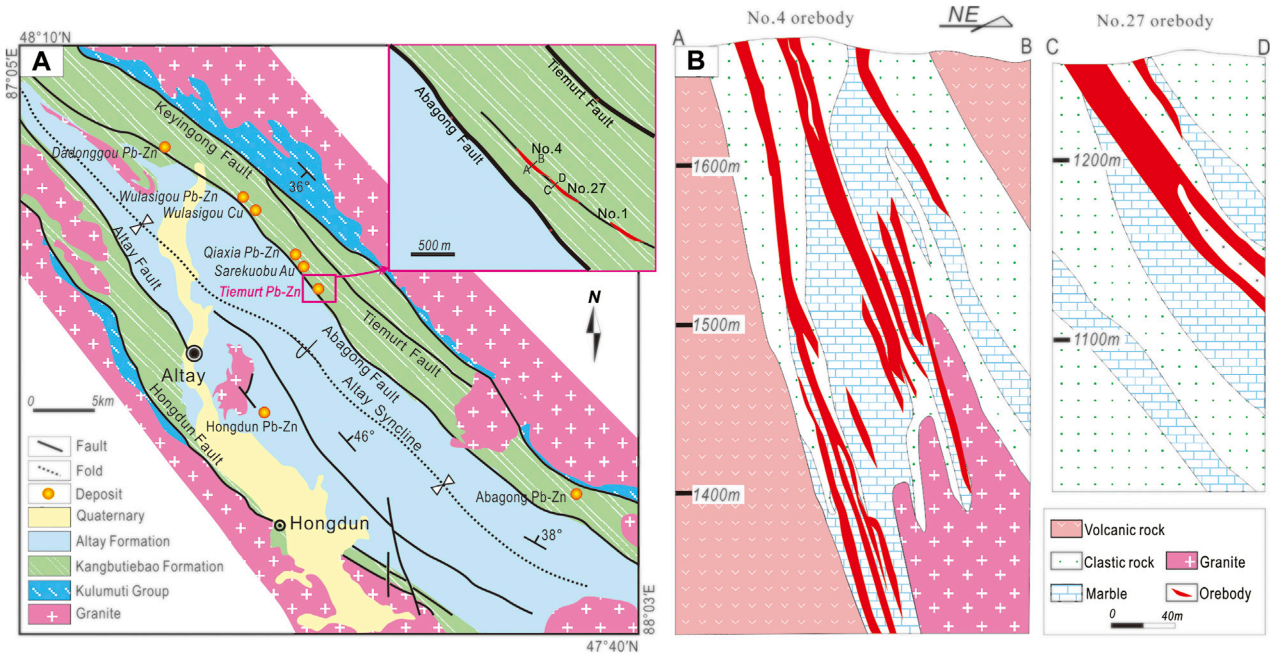

FIGURE 2 | (A) Geological map of the Kelan Basin and ore deposits, and the inserted geological map of the Tiemurt Pb–Zn–Cu deposit (modified after Geological Team 706 of the Xinjiang Bureau of Nonferrous Metals, 2000). **(B)** Geological cross sections of the Tiemurt ore bodies No. 4 and No. 27 (modified after Xinjiang Geological Team 706, 2000).

interlayered with marine carbonates with an eruptive age of ~400 Ma through zircon U–Pb dating (Chai et al., 2009; Zheng et al., 2015). Slate, greywacke, schist, and phyllite are the diagnostic rocks assemblage of the Altay Formation. In addition, all the abovementioned strata suffered regional amphibolite to greenschist-facies metamorphism during the subsequent Permian to Triassic orogenesis (Zhuang, 1994; Laurent et al., 2002). Limited Orodovician–Early Jurassic intermediate to felsic intrusions are exposed in the Kelan Basin (**Figure 2A**).

Ore Deposit Geology of the Tiemurt

The Tiemurt polymetallic deposit contains a confirmed metal reserve of Pb–Zn (0.29 million tons) and Cu (0.15 million tons), as well as economic Au (8 tons). Three principal lode ore bodies (Nos. 1, 4, and 27) accounted for ~90% of the total reserves. They are controlled by the Abagong Fault and its subordinate faults that trend to NW trending with a highly dipping angle of 49–80° (**Figure 2B**). Intensive alterations, marked by quartz, calcite, chlorite, epidote, biotite, amphibole, tremolite, and garnet, are widely presented along the ore bodies and ore-controlled faults in the ore-hosting Kangbutiebao Formation.

A majority of metallic minerals, including pyrite, galena, sphalerite, chalcopyrite, and pyrrhotite, present ore fabrics of massive, banded, disseminated, or as veinlets and breccias. Taking into account of paragenesis sequences, two major metallogenic ore-forming stages attributed to metal accumulation are identified, that is, the seafloor sedimentation and regional orogeny-related metamorphic hydrothermal activities (Yu and Zheng, 2019).

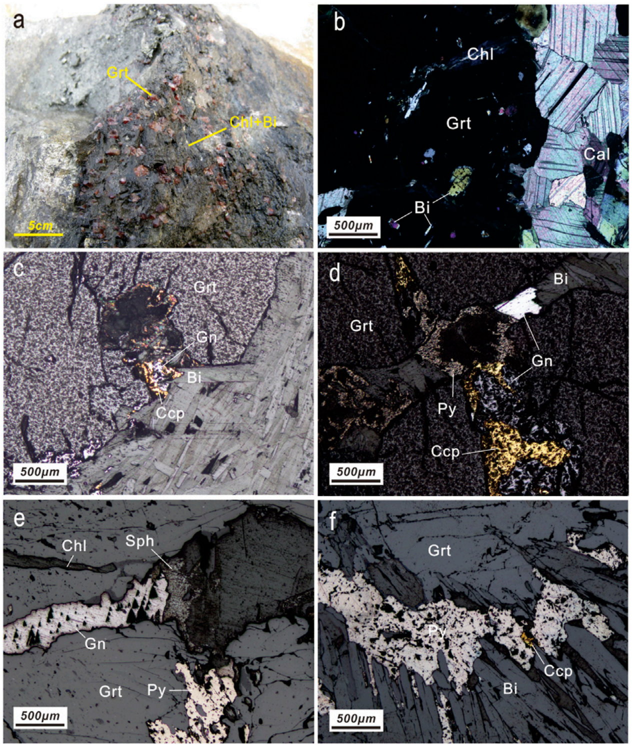

FIGURE 3 | **(A)** Reddish gem-garnet samples hosted in the greenschist from the Tiemurt deposit. **(B)** Biotite inclusion–rich Grt1 intergrown with chlorite and calcite. **(C)** and **(D)** Garnet1 coexists with chalcopyrite, chlorite, galena, and biotite. **(E)** and **(F)** Chalcopyrite, sphalerite, pyrite intergrown with garnet2, biotite, and chlorite.

SAMPLING AND ANALYTICAL METHODOLOGY

Sampling

A total of six host rock samples that contain visible garnet grains were collected from the Nos. 4 and 27 ore bodies at Tiemurt. These samples can be categorized into two types of sulfides-bearing (mineralized) and -barren (unmineralized) ones, respectively (**Figure 3**). All samples were polished into thin sections with thickness of 30 μm for petrographic study (**Figure 4**). After petrographic examination under microscope, three samples (Nos. 10TMZK-49, 10TM-26-1, and 10TM-26-2) were conducted for textural and mineral chemical analyses. Six garnet grains and their paragenetic amphibolite and biotite were analyzed to yield their textural characteristics by scanning electron microscope (SEM), as well as *in situ* major and trace elemental compositions using the coupled electron probe microanalysis (EPMA) and laser ablation–inductively coupled plasma mass spectrometry (LA-ICPMS), respectively. *In situ* LA-ICPMS and EPMA measurements were made at the same area of the minerals.

Internal Textual Analysis by SEM

After the detailed petrographic observation, we use a ΣIGMA scanning electron microscope (SEM) equipped with an X-MAX020 energy-dispersive spectrometer (EDS) that is housed at the School of the Earth Science and Geological Engineering, Sun Yat-Sen University (SYSU), to obtain internal textural information of the representative garnet grains. The instrument was operated on a backscattered electron (BSE) mode with an acceleration voltage of 20 Kv, a beam current of 20 nA, and a beam diameter of less than 1 μm.

Major Elements Analysis by EMPA

To yield major element compositions of the six garnet grains and their paragenetic amphibole, we adopted the JXA-8800 R electron probe micro analyzer (EMPA) at SYSU and the JEOL JXA-8100 EPMA at the Guangzhou Institute of Geochemistry, Chinese Academy of Science (GIG, CAS). The similar working conditions were set at an acceleration voltage of 15 kV, a beam current of 20 nA beam, and a beam diameter of 1–2 μm. Each point analysis of major elements contains a 10–20 s background acquisition (gas blank) followed by a 20 s data acquisition of the sample.

Trace Elements Analysis by LA-ICP-MS

To acquire the *in situ* minor and trace elemental compositions of garnet grains coupled with the above textures and major

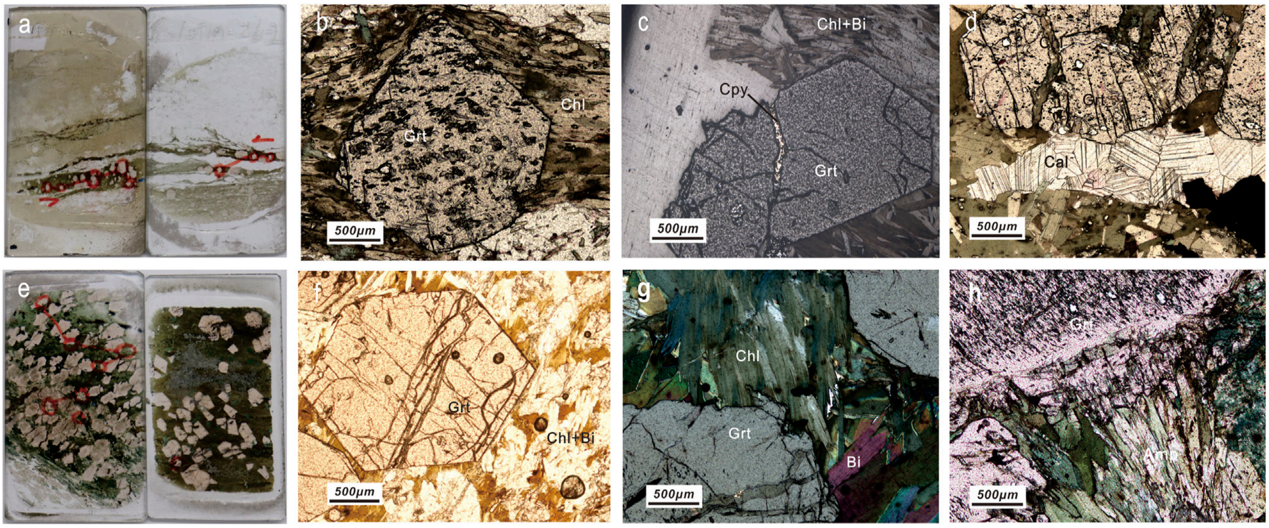

FIGURE 4 | Photographs of the garnets from the Tiemurt Pb–Zn–Cu deposit. **(A)** Thin sections (Nos. 10TM-26-1 and 10TM-26-2). **(B)** Photomicrograph of the sub- to euhedral mineral inclusion–rich Grt1 with chlorite (under the reflected light). **(C)** Photomicrographs of Grt1 garnet intergrown with chlorite and biotite, being cut by chalcopyrite veinlet (under the plane-polarized light). **(D)** Garnet grains in 10TM-26-1 intergrown with chlorite and calcite. **(E)** Thin sections (No. 10TMZK-49). **(F)** Photomicrograph of the mineral poor Grt2 intergrown with chlorite and biotite (under the cross-polarized light). **(G)** Photomicrograph of Grt2 coexisting with chlorite and biotite (under the cross-polarized light). **(H)** Garnet grains in 10TMZK-49 coexist with amphibole. Abbreviations: Amphibole = Amp, Biotite = Bi, Chalcopyrite = Cpy, Chlorite = Chl, Calcite = Cal, Chalcopyrite = Cpy, and Garnet = Grt.

elements, we operated a laser ablation–inductively coupled plasma–mass spectrometry (LA-ICP-MS) at the GIG, CAS. Each ablative spot of garnet grain was performed at the size of 47 μm in diameter, the laser repetition rate of 5 HZ, and the beam energy of ~7.2 j/cm^2 using helium as the carrier gas. The operation time include a 30 s background and a 60 s elemental information measurement. Thirty-five elements (Sc^{45}, V^{49}, Cr^{53}, Co^{59}, Ni^{60}, Cu^{63}, Zn^{66}, Ga^{69}, Rb^{85}, Sr^{88}, Y^{89}, Zr^{91}, Nb^{93}, Cs^{133}, Ba^{138}, La^{139}, Ce^{140}, Pr^{141}, Nd^{143}, Sm^{147}, Eu^{151}, Gd^{155}, Tb^{159}, Dy^{163}, Ho^{165}, Er^{166}, Tm^{169}, Yb^{173}, Lu^{175}, Hf^{178}, Ta^{181}, Pb^{208}, Th^{232}, and U^{238}) were measured. Data quantification is used in the united method of the internal standard method (Longerich et al., 1996) and the external standard of zircon 91,500 (Wiedenbeck et al., 1995). To monitor the instrumental drift, we analyzed the standard twice every 1.5 h at the condition of a 100 μm beam and a 10 Hz laser repetition rate.

RESULTS

Textural Characteristics of Garnet Grains

As illustrated in the **Table 1** and **Figure 3**, the garnet grains are commonly intergrown with amphibolite, biotite, chlorite, calcite, chalcopyrite, pyrite, and sphalerite. Most of garnet grains present euhedral to subhedral crystals with a diameter of 0.3–5 cm in diameter (**Figure 3A**). In combination with their reddish color and good transparency, they can be classified into the gem-grade garnet (**Figure 4**). No distinctive textural zonation was observed in these garnet grains in microscopic observation and in BSE imaging (**Figures 3C–F–F**, **4**, **5**).

A slight difference is identified between these garnet grain samples. The garnet grains in samples 10TM-26-1 and 10TM-26-2 are intergrown with calcite, biotite, chalcopyrite, and chlorite with a smaller grain size of 0.01–3 cm in diameter (**Figures 4A–D**). In contrast, the garnet grains in sample 10TMZK-49 coexist with chlorite, amphibole, and biotite with a diameter of 0.5–5 cm in diameter (**Figures 4E–H**).

Major Elemental Compositions

The **Supplementary Table S1** shows all the major elemental compositions of 41 spots in six representative garnet grains from three samples, and the **Table 2** presents the selected major elements with relatively high contents.

Garnet

A total of 41 EMPA spot analyses were completed on the six garnet grains, including 13 spots on sample 10TMZK-49 and 14 spots each for samples 10TM-26-1 and 10TM-26-2. The results indicate that grains in 10TMZK-49 has SiO$_2$, MnO, and FeO concentrations of 36.63–37.46 wt%, 0.79–3.65 wt%, and 31.74–35.86 wt%, respectively. The SiO$_2$, MnO, and FeO concentrations of garnets in 10TM-26-2 vary from 36.36 wt% to 37.22 wt%, 8.68 wt% to 10.90 wt%, and 22.93 to 26.36 wt%, respectively. While the grain in 10TM-26-1 vary from 36.23 wt% to 37.23 wt%, 4.29 wt% to 12.67 wt%, and 23.23 wt% to 30.02 wt %, respectively (**Table 2**).

As exhibited in the **Figure 6**, most of the garnet grains are plotted from the spectrum of spandite (spessartite–almandine) with compositions ranging from Alm$_{49.31}$Gro$_{18.42}$ to Alm$_{76.56}$Gro$_{11.}$ It is notable that no analysis is plotted in the field of spessartite + andradite + uvarovite.

TABLE 1 | Sampling description of two garnet generations in the Tiemurt deposit.

Sample No.	Position	Mineral assemblage	Size	Shape	Color
10TMZK-49	No. 4 ore body	Garnet, chlorite, biotite, amphibole, chalcopyrite, pyrite, and galena	0.5–5 cm	Euhedral to subhedral	Reddish
10TM-26-2	No. 27 ore body	Garnet, calcite, chlorite, chalcopyrite, sphalerite, and pyrite	0.01–0.3 cm	Euhedral to subhedral	Reddish
10TM-26-1	No. 27 ore body	Garnet, chlorite, calcite, chalcopyrite, sphalerite, and pyrite	0.01–0.3 cm	Euhedral to subhedral	Reddish

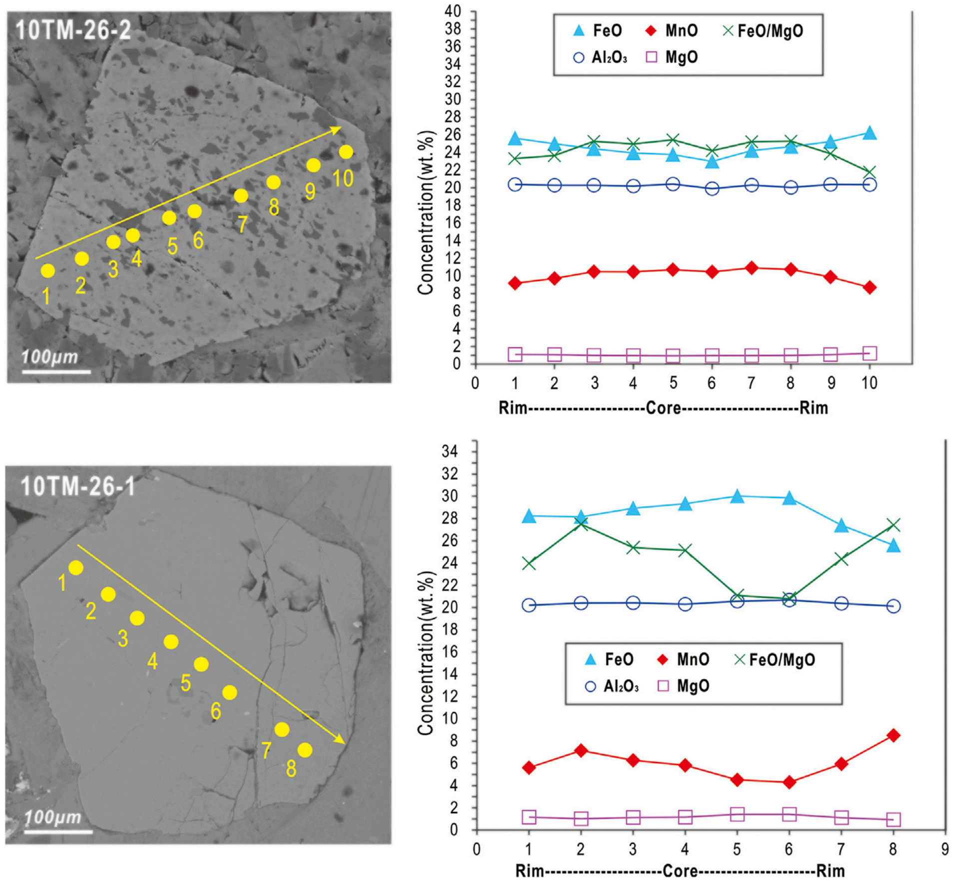

FIGURE 5 | Backscattered electron (BSE) imaging coupled with EPMA analysis on major elements profiles for Grt1 (10TM-26-2 and 10TM-26-1).

Despite homogenously isotropic textures observed in these garnet grains by BSE imaging (**Figure 5**), we conduct two profiles of major elements to examine whether they host chemical zonings. As a result, one garnet grain in 10TM-26-2 shows remarkable chemical zoning (**Figure 5A**). From core to rim, the almandine shows a significant increasing trend (56.30 mole % for rim and 49.31 mole % for core), but spessartine and grossularite show a decreasing trend from rim to core.

Different major elements show different spatial distribution pattern in the major elemental profiles (**Figure 5B**). Manganese (Mn) element is relatively enriched in the core, but iron (Fe) is enriched in the rim. In contrast, the elements of magnesium (Mg) and aluminum (Al) show no significant compositional variation from core to rim. Furthermore, the ratios of iron to magnesium (expressed by FeO/MgO) present significantly higher contents from core to rim, which is consistent with the compositional variations of spessartine and andradite.

Notably, the almandine, grossularite, and pyrope components in garnet grains are heterogeneous from core to rim. For 10TM-26-1, the contents of almandine range from 57.39 mole (%) to 64.41 mole (%) that decreases slightly from rim to core, and then decreases from core to rim (**Figure 5B**, **Table 4**). By comparison, the spessartine and andradite increase from rim to core, and then decrease from core to rim. The FeO/MnO ratios vary consistently to the almandine, grossularite, and pyrope variations. Moreover, FeO/MgO ratio variations are analogous to spessartine and andradite variations. The contents

TABLE 2 | EMPA geochemical data (wt%) of the Tiemurt garnets.

No.	10TMZK-49-G1						10TMZK-49-G2						
Id	**1**	**2**	**3**	**4**	**5**	**6**	**1**	**2**	**3**	**4**	**5**	**6**	**7**
SiO_2	37.46	36.97	37.19	36.80	36.63	36.68	36.96	37.24	37.08	37.02	36.98	37.06	36.92
TiO_2	0.04	0.03	0.02	0.00	0.00	0.01	0.03	0.04	0.02	0.00	0.00	0.00	0.05
Al_2O_3	20.68	20.52	20.50	20.52	20.37	20.14	20.38	20.59	20.48	20.61	20.70	20.44	20.41
Cr_2O_3	0.00	0.00	0.00	0.01	0.01	0.02	0.00	0.00	0.00	0.00	0.01	0.00	0.00
FeO	33.23	33.34	33.90	33.24	32.22	31.74	33.69	34.25	34.10	35.86	34.23	33.01	33.60
MnO	3.30	2.86	2.93	2.41	3.64	3.65	2.97	1.74	1.39	0.79	1.75	2.99	2.51
MgO	0.92	0.80	0.90	0.83	0.89	0.92	0.88	1.34	1.44	1.73	1.32	0.88	0.85
CaO	6.09	6.53	6.00	6.76	6.21	6.50	6.09	6.00	6.48	5.26	6.26	6.39	6.28
Total	101.73	101.04	101.43	100.58	99.97	99.66	101.00	101.20	100.99	101.27	101.23	100.77	100.61
Si	2.99	2.97	2.98	2.97	2.98	2.99	2.98	2.98	2.97	2.96	2.96	2.99	2.98
Ti	0.00	0.00	0.00	0.00	0.00	0.00	0.00	0.00	0.00	0.00	0.00	0.00	0.00
Al	1.94	1.94	1.94	1.95	1.95	1.93	1.93	1.94	1.93	1.95	1.95	1.94	1.94
Cr	0.00	0.00	0.00	0.00	0.00	0.00	0.00	0.00	0.00	0.00	0.00	0.00	0.00
Fe^{3+}	0.06	0.07	0.08	0.07	0.06	0.08	0.08	0.07	0.08	0.08	0.07	0.07	0.07
Fe^{2+}	2.16	2.17	2.20	2.18	2.12	2.08	2.19	2.22	2.20	2.32	2.22	2.15	2.20
Mn	0.22	0.19	0.20	0.17	0.25	0.25	0.20	0.12	0.09	0.05	0.12	0.20	0.17
Mg	0.11	0.10	0.11	0.10	0.11	0.11	0.11	0.16	0.17	0.21	0.16	0.11	0.10
Ca	0.52	0.56	0.52	0.59	0.54	0.57	0.53	0.51	0.56	0.45	0.54	0.55	0.54
Ura	0.00	0.01	0.00	0.04	0.04	0.06	0.00	0.00	0.00	0.00	0.02	0.00	0.00
And	3.06	3.53	3.77	3.25	3.19	3.80	3.99	3.42	4.09	3.86	3.45	3.44	3.46
Pyr	3.63	3.16	3.55	3.29	3.56	3.69	3.49	5.31	5.67	6.81	5.18	3.49	3.40
Spe	7.42	6.44	6.59	5.45	8.29	8.34	6.70	3.91	3.13	1.77	3.90	6.77	5.70
Gro	14.23	15.06	13.31	16.03	14.65	14.95	13.40	13.64	14.30	11.00	14.22	14.84	14.55
Alm	71.66	71.80	72.78	71.94	70.27	69.15	72.43	73.73	72.80	76.56	73.24	71.46	72.89
Other	0	0	0	0	0	0	0	0	0	0	0	0	0

No.	10TM-26-1-G1						10TM-26-2-G1			
Id	**1**	**2**	**3**	**4**	**5**	**6**	**1**	**2**	**3**	**4**
SiO_2	37.16	37.23	36.72	36.87	36.73	36.64	37.22	37.02	37.18	36.58
TiO_2	0.09	0.10	0.08	0.12	0.09	0.08	0.15	0.04	0.07	0.06
Al_2O_3	20.20	20.19	20.21	20.12	20.20	20.57	20.25	20.46	20.40	20.29
Cr_2O_3	0.00	0.00	0.00	0.00	0.00	0.01	0.00	0.02	0.00	0.00
FeO	25.18	23.46	23.23	24.88	24.18	24.95	24.84	26.36	25.52	25.96
MnO	10.27	12.23	12.67	10.39	11.38	11.06	10.06	8.68	8.95	9.03
MgO	0.81	0.67	0.72	0.76	0.71	0.82	0.97	1.20	1.12	1.14
CaO	7.28	7.07	6.85	7.35	6.93	6.45	7.58	6.83	7.51	6.82
Total	101.00	100.94	100.48	100.49	100.22	100.56	101.05	100.60	100.75	99.87
Si	2.98	2.99	2.97	2.98	2.97	2.96	2.98	2.98	2.98	2.97
Ti	0.01	0.01	0.01	0.01	0.01	0.00	0.01	0.00	0.00	0.00
Al	1.91	1.91	1.93	1.91	1.93	1.96	1.91	1.94	1.93	1.94
Cr	0.00	0.00	0.00	0.00	0.00	0.00	0.00	0.00	0.00	0.00
Fe^{3+}	0.10	0.09	0.09	0.10	0.09	0.06	0.10	0.07	0.08	0.08
Fe^{2+}	1.59	1.48	1.48	1.58	1.55	1.62	1.57	1.70	1.63	1.68
Mn	0.70	0.83	0.87	0.71	0.78	0.76	0.68	0.59	0.61	0.62
Mg	0.10	0.08	0.09	0.09	0.09	0.10	0.12	0.14	0.13	0.14
Ca	0.63	0.61	0.59	0.64	0.60	0.56	0.65	0.59	0.64	0.59
Ura	0.00	0.00	0.00	0.00	0.00	0.03	0.00	0.06	0.00	0.00
And	4.87	4.57	4.56	4.88	4.25	3.17	4.86	3.69	4.09	4.01
Pyr	3.20	2.66	2.85	3.04	2.85	3.23	3.83	4.77	4.43	4.56
Spe	23.17	27.68	28.67	23.53	25.85	24.93	22.64	19.56	20.15	20.46
Gro	15.90	15.69	15.04	16.17	15.67	15.20	16.72	15.71	17.30	15.54
Alm	52.84	49.39	48.87	52.37	51.38	53.44	51.96	56.20	54.03	55.43
Other	0	0	0	0	0	0	0	0	0	0

Note: All the calculations are based on 12 oxygens. Abbreviations: Ura-uvarovite, And-andradite, Pyr-pyrope, Spe-spessartine, Gro-grossular, Alm-almandine, and Amp-amphibole. "-": Below the detection limit.

of FeO are higher in core than rim, but its variations from rim to core are different. Distinctively, MnO is weakly zoned in core and it varies consistently to the FeO/MgO variations. While Al_2O_3 and MgO concentrations show no spatial variations from core to rim.

Amphibolite

Somewhat amounts of amphibole grains coexist with garnet grains in 10TMZK-49 (**Figure 4**), and two analyses of their compositions are listed in **Table 3**. They contain major compounds of SiO_2, MgO, Al_2O_3, MnO, and

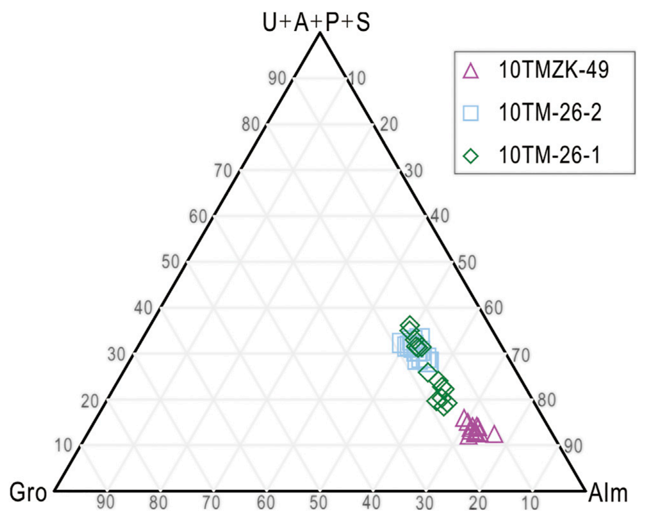

FIGURE 6 | Classification diagram for the Tiemurt garnets. Abbreviations: Gro = grossular, And = andradite, Ura = uvarovite, Pyr = pyrope, Spe = spessartine, and Alm = almandine.

FeO contents up to 40.51–51.94 wt%, 4.67–11.70 wt%, 0.32–15.01 wt %, 0.18–0.73 wt%, and 23.45–33.25 wt%, respectively.

Trace Elemental Compositions

A total of thirty (30) trace elements analyses were conducted on garnet grains in the three samples, including 10 spots in 10TMZK-49, and 20 spots in 10TM-26-1 and 10TM-26-2. The results are listed in the **Table 5**, and the spike diagrams of rare earth elements (REEs) are plotted in the **Figure 7**, and the spike and statistical column diagrams of trace elements are displayed in the **Figure 8**.

The garnet grains in three samples show similar chondrite-normalized REE patterns. High rare-earth elements (HREE) are relatively enriched with the ∑HREE values of 21.43–101.98 ppm (mean = 41.65 ppm). Moreover, the values of ∑LREE/∑HREE is extremely low (0.03–0.13, mean = 0.071). The feature of cerium negative anomaly (δCe = 0.11–4.17, mean = 0.58) and europium positive anomalies (Eu/Eu* = 1.28–2.57, mean = 1.66) is also identified.

In addition, the large-ion lithophile elements (LILE) are extremely depleted in all garnet grains, with negligible amounts of Rb, Sr, and Ba, much lower than the value of average primitive mantle (Sun and McDonough, 1989; **Figure 8**). By contrast, the high-field elements (HFS), such as Th, Zr, and Y, are relatively enriched in the Tiemurt garnet than the values of average primitive mantle (**Figure 8**). As for the trace elements of P, Sm, and Ti, both the Tiemurt garnet and average primitive mantle show no obvious distinction in concentrations (**Figure 8**).

DISCUSSION

Mineral Growth History and Origin of Garnet

The systematic textural and chemical characteristics provide solid evidence for our discussion on mineral growth history and origin of the Tiemurt gem-grade garnet grains (Vander and Andre, 1991; Zhao et al., 1999; Martin et al., 2011). During the mineral growing, the garnet can grow to geo grade under the conditions of 1) the adequate influx supplying and 2) large enough growth space (Hickmott and Spear, 1992; Baxter et al., 2013). Our garnet displays relatively coarse and euhedral grains (**Figure 3A**), indicative of a well-supplied open space. However, the origin of Tiemurt garnet, such as mantle, ocean crust, skarn metasomatism, sedimentary exhalation, or metamorphism, needs to be discussed in detail (Gemmell et al., 1992; Hoal et al., 1994; Burton et al., 1999).

In the skarn deposit, the magmatic-hydrothermal fluids replace host carbonates to facilitate growth of gem-grade garnet (Jeremy and Hamid, 2013). In this case, the skarn garnet universally hosts some clear occasional zonation because of the relatively low rate of the metasomatic process (Vander and Andre, 1991; Park et al., 2017). In fact, the growth rate also acts as an important factor in controlling the grain size as well as the zonation pattern of garnet (Jamtveit and Hervig, 1994; García-Ruiz and Otálora, 2015). No textual zonation in the Tiemurt garnet implies a relatively high growth rate, which also exclude their possibility of magmatic-hydrothermal origin analogy to skarn (Jamtveit, 1991; Jamtveit et al., 1993; Zang et al., 2019).

The chemical compositions further provide reliable evidences for the garnet origin (Zhai et al., 2014; An et al., 2017). It is consensus that an abundance of Fe and Mn is distributed in the seawater, and therefore the garnet with sedimentary exhalation origin is Fe and Mn rich for their incorporation into the garnet crystal lattices (Gemmell et al., 1992; Burton et al., 1999). For the Tiemurt garnet, the feature of Al and Fe rich but Ca and Mn depleted are not products of seafloor sedimentation (Zheng et al., 2013a). Considering that no rocks related to the mantle transition zone or subducting ocean crust have been reported in the region, the only possible origin for the Tiemurt garnet is metamorphic.

In fact, the variations of geological occurrence, mineral assemblages, mineralogy, textures, and chemistry between Grt1 and Grt2 are just caused by the orogeny-related metamorphism and deformation (Chen et al., 2012; Zheng

TABLE 3 | EMPA geochemical data (wt%) of the Tiemurt amphibole.

No.	10TMZK-49	
Id	1	2
K_2O	0.44	0.52
Na_2O	1.18	1.01
SiO_2	40.51	41.13
TiO_2	0.15	0.12
Al_2O_3	15.01	14.13
FeO	23.75	23.45
MgO	4.67	5.46
MnO	0.2	0.18
CaO	11.45	11.43
Total	97.33	97.22

TABLE 4 | EMPA geochemical data (wt%) of the two generation garnet profiles.

No.	**10TM-26-2-G2**									
Id	**1 (Rim)**	**2**	**3**	**4**	**5 (Core)**	**6 (Core)**	**7**	**8**	**9**	**10 (Rim)**
SiO_2	36.84	36.79	36.85	36.82	36.89	36.36	36.83	36.78	36.79	36.78
TiO_2	0.02	0.06	0.04	0.03	0.04	0.04	0.07	0.09	0.05	0.05
Al_2O_3	20.36	20.27	20.29	20.19	20.42	19.90	20.30	20.02	20.36	20.34
Cr_2O_3	0.03	0.02	0.02	0.00	0.01	0.00	0.00	0.02	0.00	0.00
FeO	25.61	24.96	24.39	23.91	23.74	22.96	24.20	24.64	25.22	26.22
MnO	9.16	9.71	10.47	10.44	10.69	10.45	10.90	10.73	9.86	8.69
MgO	1.10	1.06	0.97	0.96	0.94	0.95	0.96	0.98	1.06	1.20
CaO	7.12	7.31	7.32	7.41	7.46	7.82	7.25	6.81	7.01	6.68
Total	100.24	100.16	100.35	99.76	100.17	98.48	100.52	100.06	100.35	99.97
Si	2.97	2.97	2.97	2.98	2.98	2.98	2.97	2.98	2.97	2.98
Ti	0.00	0.00	0.00	0.00	0.00	0.00	0.00	0.01	0.00	0.00
Al	1.94	1.93	1.93	1.93	1.94	1.92	1.93	1.91	1.94	1.94
Cr	0.00	0.00	0.00	0.00	0.00	0.00	0.00	0.00	0.00	0.00
Fe^{3+}	0.08	0.09	0.09	0.08	0.07	0.09	0.09	0.10	0.08	0.07
Fe^{2+}	1.65	1.60	1.56	1.54	1.53	1.49	1.54	1.57	1.62	1.70
Mn	0.63	0.66	0.72	0.72	0.73	0.73	0.74	0.74	0.67	0.60
Mg	0.13	0.13	0.12	0.12	0.11	0.12	0.12	0.12	0.13	0.15
Ca	0.62	0.63	0.63	0.64	0.64	0.69	0.63	0.59	0.61	0.58
FeO/MgO	23.26	23.68	25.15	24.85	25.31	24.12	25.10	25.17	23.79	21.78
Ura	0.09	0.06	0.05	0.00	0.03	0.01	0.00	0.06	0.00	0.00
And	3.87	4.23	4.29	4.07	3.50	4.35	4.45	4.90	4.06	3.66
Pyr	4.38	4.21	3.86	3.85	3.74	3.86	3.83	3.92	4.21	4.81
Spe	20.70	21.96	23.66	23.77	24.19	24.05	24.57	24.40	22.26	19.71
Gro	16.40	16.62	16.59	17.27	17.82	18.42	16.24	14.63	15.96	15.52
Alm	54.56	52.92	51.56	51.04	50.72	49.31	50.91	52.09	53.50	56.30
Other	0	0	0	0	0	0	0	0	0	0

No.	**10TM-26-1-G2**							
Id	**1**	**2**	**3**	**4 (Core)**	**5 (Core)**	**6**	**7**	**8 (Rim)**
SiO_2	36.82	37.05	36.79	36.87	36.98	36.70	36.26	36.23
TiO_2	0.04	0.06	0.05	0.03	0.03	0.04	0.06	0.09
Al_2O_3	20.22	20.42	20.43	20.31	20.59	20.70	20.39	20.14
Cr_2O_3	0.01	0.02	0.00	0.00	0.00	0.04	0.02	0.00
FeO	28.24	28.15	28.93	29.35	30.02	29.87	27.41	25.61
MnO	5.61	7.15	6.28	5.83	4.52	4.29	5.94	8.51
MgO	1.18	1.02	1.14	1.17	1.42	1.43	1.13	0.93
CaO	6.65	6.82	6.93	6.97	6.96	7.30	6.64	6.45
Total	98.77	100.69	100.56	100.52	100.52	100.37	97.85	97.97
Si	3.01	2.98	2.96	2.97	2.97	2.95	2.99	2.99
Ti	0.00	0.00	0.00	0.00	0.00	0.00	0.00	0.01
Al	1.95	1.94	1.94	1.93	1.95	1.96	1.98	1.96
Cr	0.00	0.00	0.00	0.00	0.00	0.00	0.00	0.00
Fe^{3+}	0.05	0.07	0.08	0.09	0.07	0.06	0.02	0.04
Fe^{2+}	1.88	1.82	1.87	1.89	1.95	1.95	1.87	1.72
Mn	0.39	0.49	0.43	0.40	0.31	0.29	0.41	0.60
Mg	0.14	0.12	0.14	0.14	0.17	0.17	0.14	0.11
Ca	0.58	0.59	0.60	0.60	0.60	0.63	0.59	0.57
FeO/MgO	23.98	27.49	25.40	25.15	21.08	20.84	24.37	27.42
Ura	0.04	0.05	0.00	0.00	0.00	0.11	0.07	0.01
And	2.43	3.71	4.01	4.43	3.37	3.07	1.12	2.19
Pyr	4.79	4.07	4.51	4.63	5.64	5.65	4.60	3.82
Spe	12.96	16.16	14.14	13.13	10.17	9.62	13.80	19.81
Gro	16.96	15.72	15.71	15.45	16.43	17.50	18.33	16.78
Alm	62.82	60.30	61.63	62.36	64.41	64.04	62.09	57.39
Other	0	0	0	0	0	0	0	0

Note: All the calculations are based on 12 oxygens. Abbreviations: Ura-uvarovite, And-andradite, Pyr-pyrope, Spe-spessartine, Gro-grossular, Alm-almandine, and Amp-amphibole. "-": Below the detection limit.

et al., 2013a). In the early stage of orogenesis, the wall rocks are highly foliated to form garnet schists (Grt1). As the orogenesis continues, the ongoing structural development and accompanying large-scale fluid activities cause destruction of Grt1 and Grt2 precipitations in the larger host space. This mineral growth process is recorded by the variations of grain size, micromineral inclusions, and mineral assemblages between Grt1 and Grt2.

Physicochemical Condition Recorded by Garnet

Under the metamorphic environment, we can utilize the contents and variations of Ca, Mn, Fe, and Mg in garnet to evaluate the pressure (P)–temperature (T) condition (Andrew, 1994; Gerya et al., 1997). The principle is that the P-T condition has an impact on cooperation of these cations into crystal structures of garnet in relation with anions' charge and radius (Shannon, 1976; Smith et al., 2004; Xia et al., 2016). For the same (II) charge substituting to the "A" location, the decreasing order of anions radius $Ca^{2+} > Mn^{2+} > Fe^{2+} > Mg^{2+}$ is sensitive to reflect the fluctuation of the P-T condition (Zhou et al., 2014), that is, Ca-rich garnet formed in low-pressured contact metamorphism, Mn-Al–rich garnet formed in low-grade regional metamorphism, Fe-Al–rich garnet formed in relatively higher regional metamorphism, and Mg-rich garnet formed in high-pressured metamorphism (Yardley et al., 1991; Jamtveit et al., 1993; Crowe et al., 2001; Fernando et al., 2003). Therefore, the Tiemurt Fe-Al–rich garnet is formed in relatively higher regional metamorphism. In consideration of regional geology (Chen et al., 2012), the low-amphibolite to middle-greenschist facies are the preferred window for the Tiemurt garnet.

Amphibole is a common mineral of metabasites from amphibolite to greenschist facies, and its composition changes regularly with metamorphic grade (Triboulet, 1992). The amphibole paragenetic with garnet allows us to calculate more accurate P-T condition (Gerya et al., 1997). Here, we adopt the methodology of Gerya et al. (1997) based on the Gibbs' phase rule at mineral equilibrium (Holland and Blundy, 1994; Gerya et al., 1997). The calculation is based on the following formula derivation, that is,

$$T(K) = \frac{6119 - 28.4P + 114X_{Mg}^{Hbl}}{8.181 - Rln(8.489 - Si^{Hbl})}$$

$$P(kbr) = \left[2543 - 4.744T + 175X_{Mg}^{Hbl} + RTln\left(Al^{Hbl} + 1.433\right)\right] \times \Big/ 148.1,$$

where P = P, kbar; T = T, K; $X_{Mg}^{Hbl} = Mg/(Fe + Mg)$, bulk Mg mole fraction of amphibole; and Si^{Hbl} and Al^{Hbl} are Si and Al in amphibole calculated on 13 cations.

The calculated temperature range of 10TMZK-49 is 640–643°C at the pressure of 5,218–5,900 bar (**Table 6**).

Additionally, we can use the distribution patterns of REE and trace elements to further deduce the acidity and redox condition (Sverjensky, 1984; Bau, 1991). It is suggested that REE fractionation is strongly dependent on the hydrothermal fluid pH (Bau, 1991), HREE enrichment, and LREE depletion with weak negative or no Eu anomalies indicating a nearly neutral environment. Garnet from the Tiemurt is characterized as HREE-rich, LREE-depleted, and weak positive Eu anomaly (**Figure 7**). Fractionation of HREE against LREE is controlled by the major compositions such as Al and Fe in garnet, and the weak positive Eu anomaly is caused by the metamorphic hydrothermal fluids under mildly acidic condition (Scherer et al., 2000; Pertermann et al., 2004; Schmidt et al., 2011; Cheng et al., 2012). In this case, the REE pattern is chiefly determined by the complex agents (e.g., Cl^{-}) that enhance stability of Eu^{2+}, rather than REE^{3+}, in solution (Geiger et al., 1989; Ballaran et al., 1999), which can produce distinct positive Eu anomalies. The presence of chlorite intergrown with garnet also supports the mildly acidic condition, which facilitates soluble Eu^{2+} transporting and substituting Fe^{2+} in garnet crystal to form distinctly positive Eu anomalies (Smith et al., 2004; Gaspar et al., 2008).

Another evidence is the concentrations of uranium, which is a redox-sensitive element with different valence states of U^{4+} and U^{6+} (Smith et al., 2004; Zhang et al., 2017b). The decrease of fO_2 in the hydrothermal fluids reduces the solubility of U and increases the incorporation of U into Garnet. It means that the higher U contents of garnet may indicate the lower fO_2 of hydrothermal fluids. At the Tiemurt, Grt1 has lower U contents (0.0002–0.19 ppm) than those of Grt2 (0.02–12.5 ppm), which partly indicate that Grt1 hosts higher fO_2.

Additionally, the iron electrovalence ratio (Fe^{2+}/Fe^{3+}) is also an important oxygen fugacity indicator of garnet (Park et al., 2017; Liang et al., 2021). For the garnet $A_3B_2(SiO_4)_3$ formula, the cations of Fe^{2+} and Fe^{3+} can be accommodated into the crystal structure of A and B, respectively. For the B location, both Al^{3+} and Fe^{3+} can occupy together, and therefore Al-rich chemical composition can reduce the amount of Fe^{3+} (Jamtveit et al., 1993). In the Tiemurt garnet, Grt1 yields a more Al-rich chemical composition that can be calculated into the equal Fe^{2+}/Fe^{3+} ratios of 15.9–23.1, distinct from Grt2 with a higher Fe^{2+}/Fe^{3+} ratio of 21.1–83.3. Therefore, the variation of Fe^{2+}/Fe^{3+} from Grt1 to Grt2 records a significant decreasing trend of oxygen fugacity at the Tiemurt.

Furthermore, the enrichment of Th, Y, and HREE indicates a relatively reduced condition in Grt2 (Gaspar, 2005). Taking the element of Th for an example, the decreasing fO_2 value of the fluid system could reduce Th solubility in solution and in turn increase Th incorporation into garnet (Huang et al., 2014).

Metamorphic Garnet Linking With the Orogenic-Type Deposits in Altay

On the basis of above discussion, the garnets from the Tiemurt deposit are principally crystallized from the metamorphic hydrothermal fluids, and therefore the variations in garnet geochemistry are largely controlled by some external factors such as fluid compositions, fluid–rock interactions, and metasomatism dynamics (Jamtveit, 1991; Ottonello et al., 1996; Ottonello and Moretti, 1998; Gaspar et al., 2008). Grt1 and Grt2 host the similar fluid origin and fluid–rock interaction ratios, and therefore their chemical variations are possibly caused by metasomatism dynamics, that is, diffusive or infiltration metasomatism (Bau, 1991; Gaspar et al., 2008). The diffusive metasomatism will produce fluids with near-neutral pH and alteration products in which REE composition is buffered by the composition of the host rocks due to long pore fluid residence under closed-system conditions (Dziggel et al., 2009; Zhang et al., 2017a; Xiao et al., 2018). While the infiltration metasomatism, associated with an increase in fluid–rock interaction ratios, will produce fluids and mineral assemblages buffered by reduced, mildly acidic, external-derived fluids, where chloride complexes

TABLE 5 | Representative LA-ICP-MS data (ppm) of garnets from the Tiemurt deposit.

No.	**GT1**									
Id	**1**	**2**	**3**	**4**	**5**	**6**	**7**	**8**	**9**	**10**
Trace element										
Sr	0.021	0.000	0.000	0.033	0.011	0.000	0.000	0.042	0.025	0.020
Rb	0.000	0.042	0.000	0.000	0.010	0.001	0.025	0.064	0.022	0.000
Ba	0.000	0.000	0.000	0.030	0.028	0.059	0.052	0.000	0.000	0.000
Th	0.000	0.002	0.000	0.014	0.164	0.031	0.028	0.245	0.010	0.000
U	0.012	0.026	0.000	0.591	1.516	0.584	0.375	0.073	0.049	0.023
Ta	0.000	0.010	0.000	0.004	0.000	0.002	0.000	0.009	0.000	0.043
Nb	0.000	0.002	0.000	0.000	0.044	0.052	0.013	0.001	0.000	0.000
P	33.537	40.304	40.537	32.427	34.267	38.722	36.034	36.842	32.796	37.750
Zr	3.578	3.942	3.773	68.137	143.078	42.672	30.271	4.199	4.638	4.172
Hf	0.016	0.040	0.058	1.766	3.072	1.204	0.674	0.102	0.119	0.045
Ti	46.466	55.841	56.164	44.927	47.477	53.649	49.925	51.044	45.438	52.303
Y	94.569	92.279	66.469	77.404	54.408	66.340	54.650	40.667	52.979	80.598
REE										
La	0.000	0.000	0.000	0.000	0.054	0.000	0.031	0.016	0.000	0.000
Ce	0.244	0.010	0.021	0.000	0.050	0.088	0.023	0.060	0.051	0.019
Pr	0.117	0.173	0.230	0.059	0.127	0.000	0.097	0.283	0.189	0.237
Nd	0.739	0.763	0.839	1.008	0.807	0.774	0.275	0.395	0.253	0.379
Sm	9.024	10.390	9.865	10.042	11.036	8.402	11.575	9.710	11.049	10.367
Eu	26.575	29.058	26.545	29.117	26.642	28.363	29.007	29.237	29.933	26.730
Gd	32.409	31.830	29.613	31.123	27.296	29.138	31.245	26.526	30.765	29.781
Tb	36.030	37.053	33.286	33.791	27.393	29.324	28.226	24.437	26.902	36.701
Dy	47.151	46.328	35.571	39.922	26.586	34.811	30.429	24.912	29.826	40.725
Ho	57.155	55.752	38.859	45.130	30.698	38.012	30.829	23.533	29.352	44.864
Er	74.422	67.941	43.026	56.392	34.987	46.962	38.052	27.968	34.977	62.542
Tm	90.430	78.550	46.163	66.192	40.166	53.914	46.190	29.713	35.729	77.801
Yb	102.935	91.637	46.231	76.022	47.549	59.567	55.507	34.404	35.686	91.758
Lu	107.189	93.968	47.398	80.941	47.926	65.647	63.035	34.474	35.072	105.836
ΣREE	584.420	543.452	357.646	469.739	321.316	395.001	364.522	265.668	299.784	527.741
LREE	36.699	40.394	37.501	40.226	38.715	37.627	41.009	39.702	41.475	37.732
HREE	547.721	503.058	320.146	429.513	282.601	357.374	323.514	225.966	258.309	490.008
LREE/HREE	0.067	0.080	0.117	0.094	0.137	0.105	0.127	0.176	0.161	0.077
LaN/YbN	0.000	0.000	0.000	0.000	0.001	0.000	0.000	0.000	0.000	0.000
δEu	4.229	4.497	4.388	4.625	4.482	4.972	4.393	5.236	4.651	4.334
δCe	0.647	0.018	0.029	0.000	0.103	0.590	0.066	0.065	0.084	0.025

No.	**GT2**									
Id	**1**	**2**	**3**	**4**	**5**	**6**	**7**	**8**	**9**	**10**
Trace element										
Sr	0.024	0.014	0.046	0.017	0.000	0.010	0.000	0.037	0.000	0.000
Rb	0.034	0.000	0.000	0.000	0.012	0.000	0.053	0.019	0.030	0.013
Ba	0.000	0.042	0.000	0.017	0.000	0.000	0.000	0.013	0.015	0.051
Th	0.289	0.223	0.007	0.006	0.018	0.000	0.588	0.016	0.121	0.012
U	2.241	1.553	0.056	0.037	0.021	0.019	12.527	0.000	1.246	0.000
Ta	0.000	0.000	0.005	0.025	0.009	0.000	0.029	0.002	0.026	0.012
Nb	0.000	0.000	0.012	0.032	0.035	0.025	0.022	0.032	0.015	0.000
P	40.747	32.876	37.976	31.987	38.109	32.096	36.587	36.815	37.197	36.800
Zr	167.055	110.385	4.163	3.830	4.450	6.404	1,350.733	4.528	114.192	3.518
Hf	4.305	2.837	0.000	0.130	0.216	0.088	35.570	0.045	2.872	0.074
Ti	56.455	45.550	52.615	44.317	52.800	44.469	50.691	51.008	51.536	50.986
Y	34.559	62.959	111.729	93.450	150.614	128.534	139.929	102.712	108.036	82.849
REE										
La	0.000	0.031	0.000	0.000	0.021	0.000	0.000	0.111	0.043	0.029
Ce	0.032	0.056	0.000	0.005	0.039	0.061	0.004	0.018	0.037	0.021
Pr	0.225	0.211	0.000	0.000	0.000	0.000	0.025	0.000	0.000	0.028
Nd	0.000	0.378	0.953	0.498	0.452	0.309	0.632	0.000	0.173	0.937
Sm	7.080	5.596	5.367	8.865	9.607	9.118	9.526	6.099	7.795	5.553
Eu	21.915	21.530	22.508	25.412	27.075	28.145	26.841	25.004	24.334	21.353
Gd	19.620	23.900	28.772	28.740	32.100	29.660	30.044	27.967	25.659	27.271
Tb	17.696	28.649	36.197	36.040	42.895	37.396	42.376	36.991	34.451	30.589
Dy	16.733	31.967	50.877	45.802	59.839	52.838	61.972	45.593	46.816	40.309

(Continued on following page)

TABLE 5 | (*Continued*) Representative LA-ICP-MS data (ppm) of garnets from the Tiemurt deposit.

No.	**GT2**									
Id	**1**	**2**	**3**	**4**	**5**	**6**	**7**	**8**	**9**	**10**
Ho	16.564	32.037	62.313	52.091	82.521	68.587	83.550	55.819	60.413	44.990
Er	23.856	42.635	84.099	65.940	129.771	109.202	115.769	76.993	85.242	64.704
Tm	28.860	50.128	105.204	84.622	179.313	152.400	145.646	99.616	114.065	81.839
Yb	34.537	63.975	131.639	99.817	239.726	205.976	190.661	122.911	156.172	105.187
Lu	39.003	71.522	147.738	113.165	279.686	247.076	223.939	139.362	182.381	122.095
ΣREE	226.121	372.613	675.667	560.998	1,083.044	940.768	930.983	636.485	737.582	544.906
LREE	29.252	27.801	28.828	34.780	37.194	37.633	37.027	31.232	32.383	27.922
HREE	196.869	344.812	646.839	526.218	1,045.850	903.135	893.956	605.253	705.199	516.985
LREE/HREE	0.149	0.081	0.045	0.066	0.036	0.042	0.041	0.052	0.046	0.054
LaN/YbN	0.000	0.000	0.000	0.000	0.000	0.000	0.000	0.001	0.000	0.000
δEu	5.331	4.856	4.433	4.430	4.263	4.759	4.440	4.900	4.773	4.357
δCe	0.044	0.078	-	0.177	0.378	0.778	0.046	0.128	0.366	0.163

No.	**GT3**									
Id	**1**	**2**	**3**	**4**	**5**	**6**	**7**	**8**	**9**	**10**
Trace element										
Sr	0.027	0.009	0.000	0.039	0.000	0.021	0.000	0.000	0.001	0.000
Rb	0.039	0.000	0.036	0.031	0.000	0.000	0.028	0.008	0.000	0.030
Ba	0.032	0.035	0.027	0.000	0.034	0.000	0.000	0.001	0.000	0.000
Th	0.046	0.127	0.381	0.021	0.015	0.156	0.708	0.066	0.000	0.011
U	0.096	1.487	4.145	0.107	0.134	2.505	9.938	0.825	0.087	0.187
Ta	0.009	0.000	0.007	0.000	0.022	0.007	0.034	0.015	0.003	0.012
Nb	0.000	0.002	0.035	0.031	0.031	0.009	0.082	0.035	0.102	0.028
P	34.733	34.420	40.483	44.056	36.789	33.070	38.216	29.967	31.515	36.069
Zr	7.050	148.967	325.363	11.300	11.735	234.233	1,125.763	67.664	5.868	11.284
Hf	0.172	4.166	8.708	0.181	0.293	5.863	29.051	1.799	0.136	0.205
Ti	48.123	47.689	56.090	61.039	50.972	45.818	52.949	41.519	43.664	49.974
Y	43.349	48.502	57.178	46.032	59.583	58.396	59.344	63.203	43.397	46.229
REE										
La	0.004	0.000	0.171	0.001	0.000	0.000	0.000	0.001	0.078	0.088
Ce	0.000	0.000	0.028	0.012	0.000	0.000	0.035	0.045	0.043	0.023
Pr	0.154	0.127	0.168	0.221	0.134	0.070	0.073	0.034	0.088	0.109
Nd	0.889	0.603	0.583	0.371	1.228	0.468	0.462	1.071	0.399	0.000
Sm	7.839	7.455	8.631	6.307	6.746	9.058	7.869	7.877	7.461	7.220
Eu	25.843	27.598	28.016	30.971	31.776	27.403	31.706	29.707	27.020	25.975
Gd	20.512	18.911	19.893	20.635	17.984	17.304	18.565	20.681	18.495	16.513
Tb	18.235	19.282	19.973	18.205	21.001	19.854	21.015	21.913	17.879	18.656
Dy	20.742	21.961	25.614	20.717	24.393	25.567	25.423	26.029	19.038	20.580
Ho	22.719	25.962	29.688	24.018	31.818	32.106	32.044	35.861	23.446	25.675
Er	28.306	35.793	45.119	34.266	52.625	49.464	48.706	54.634	33.124	37.628
Tm	38.475	48.965	57.556	43.967	71.233	66.136	65.387	76.081	45.260	53.363
Yb	45.297	57.665	68.263	52.262	93.460	82.534	82.415	108.278	57.090	65.256
Lu	47.006	69.847	76.029	56.348	108.956	93.387	100.252	126.359	58.463	71.436
ΣREE	276.021	334.170	379.732	308.300	461.354	423.351	433.950	508.573	307.885	342.521
LREE	34.728	35.784	37.597	37.882	39.884	36.999	40.144	38.736	35.091	33.415
HREE	241.293	298.386	342.135	270.418	421.470	386.352	393.806	469.836	272.795	309.107
LREE/HREE	0.144	0.120	0.110	0.140	0.095	0.096	0.102	0.082	0.129	0.108
LaN/YbN	0.000	0.000	0.002	0.000	0.000	0.000	0.000	0.000	0.001	0.001
δEu	5.900	6.761	6.305	7.540	8.326	6.589	7.712	6.734	6.715	7.022
δCe	0.190	0.000	0.037	0.017	0.000	0.000	0.150	0.403	0.112	0.050

Note: REE normalized to chondrite (Sun and McDonough, 1989). "-": Below the detection limit.

can be important in Eu^{2+} transport (Bau, 1991; Yardley et al., 1991; Lottermoser, 1992).

Since the Tiemurt garnet formed under mildly acidic and relatively reduced condition, we inferred that they have formed by advective metasomatism (Gaspar, 2005), that is, diffusive metasomatism by fluids equilibrated with the host rocks. In this case, Grt1 and cores of Grt2 are formed by advective metasomatism, while rims of Grt2 are formed by the episodic inflections between infiltration metasomatism and advective metasomatism (Meinert et al., 2005; Dziggel et al., 2009).

As the Tiemurt garnets are spatially close to the polymetallic ores, their formation has potential to code the ore genesis of the Tiemurt deposit. A diversity of genetic types has been suggested for the ore genesis of the Pb–Zn–Cu–Au deposit in the Chinese

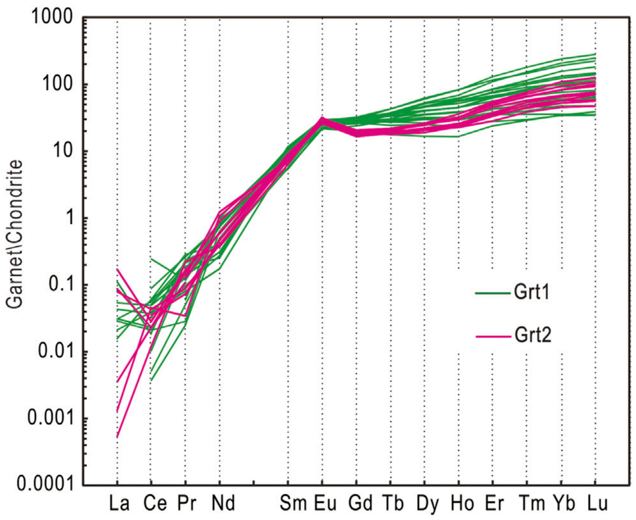

FIGURE 7 | Chondrite-normalized REE patterns of garnets from the Tiemurt deposit determined by LA-ICP-MS.

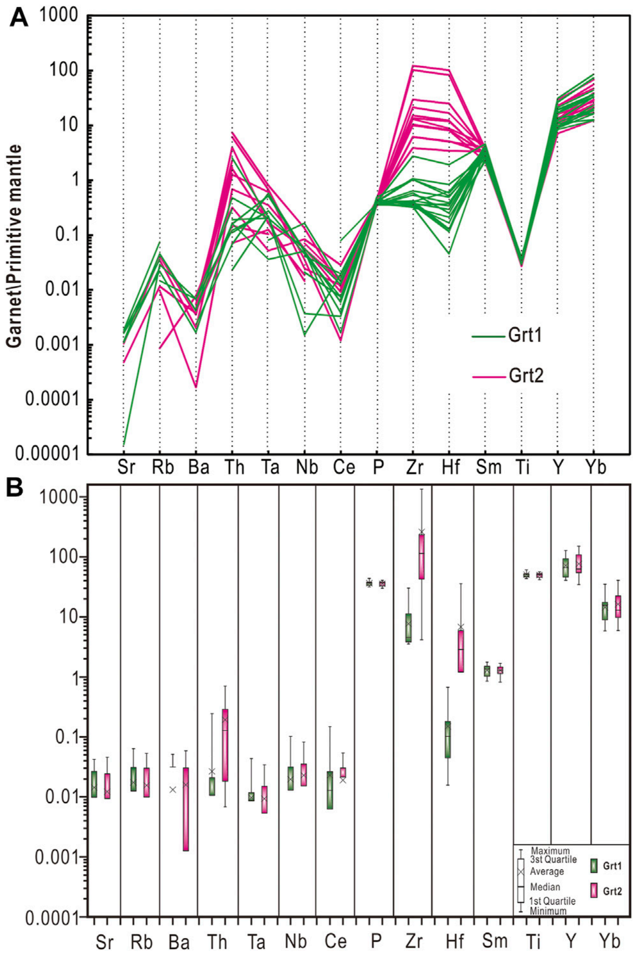

FIGURE 8 | (A) Primitive mantle-normalized multielement diagram and **(B)** the statistical column diagram of trace elements of the Tiemurt garnets.

TABLE 6 | Calculation results of the amphibole pressure and temperature.

Samples	Input T (°C)	Input P (bar)	T (calc) (°C)	P (calc) (bar)
10TMZK-49	623	5,900	643	5,900
10TMZK-49	640	5,028	640	5,218

Altay Orogen, such as VMS, metamorphosed VMS, and orogenic-type deposits (Xu et al., 2008; Xu et al., 2011; Wan et al., 2010a; Zhang et al., 2012; Zheng et al., 2013b). The key to resolve these disagreements lies in the origin of their ore fluids. The metamorphic garnet supporting the polymetallic deposits are orogenic-type, and therefore the eventual metal accumulation is attributed for the orogeny-related metamorphism and deformation, as well as the metamorphic hydrothermal fluids' activities.

CONCLUSION

1) Two categories of almandine (Fe-Al–garnet), Grt1 and Grt2, both have similar major elemental compositions (such as SiO_2, Al_2O_3, and CaO), chondrite-normalized REE patterns (HREE-enriched, LREE-depleted, Ce negative anomaly, and Eu positive anomalies), depleted lithophile elements, and enriched high-field elements.
2) The sub- to euhedral mineral inclusion–rich Grt1 is intergrown with amphibolite, chlorite, and biotite; the sub- to euhedral mineral poor Grt2 is paragenetic with quartz, calcite, chlorite, and biotite. Grt1 and Grt2 assembles and trace elements recorded a methosthermal, high-pressured, mildly acidic, and reductive condition.
3) Grt1 and cores of Grt2 are formed by advective metasomatism, while rims of Grt2 are formed by the episodic inflections between infiltration metasomatism and advective metasomatism, and their formation linking with orogeny-type regional metamorphism as well as the metamorphic hydrothermal fluids' activities.

DATA AVAILABILITY STATEMENT

The original contributions presented in the study are included in the article/**Supplementary Material**; further inquiries can be directed to the corresponding author.

AUTHOR CONTRIBUTIONS

ZH prepared samples for analysis, performed initial data analysis, and took the lead on writing the manuscript. YZ and PY wrote the final version of the manuscript. ZH was responsible for the statistical treatment of the data. YZ, YW, and CW took part in the fieldwork and developing the original ideas.

FUNDING

This study was jointly funded by the National Natural Science Foundation of China (Nos. U1803115, 41872193, and 42022020) and Natural Science Foundation of Guangdong Province (Nos. 2018B030306021 and 2016ZT06N331).

ACKNOWLEDGMENTS

Prof Chen YJ (Peking University) is thanked for his field assistance and writing guidance. We also appreciate the editor and two reviewers for their constructive suggestions and comments.

SUPPLEMENTARY MATERIAL

The Supplementary Material for this article can be found online at: https://www.frontiersin.org/articles/10.3389/feart.2021.683312/full#supplementary-material

REFERENCES

An, Y., Huang, J.-X., Griffin, W. L., Liu, C., and Huang, F. (2017). Isotopic Composition of Mg and Fe in Garnet Peridotites from the Kaapvaal and Siberian Cratons. *Geochimica et Cosmochimica Acta* 200, 167–185. doi:10.1016/j.gca.2016.11.041

Andrew, A. S. (1994). “Regional Metamorphism within a Creationist Framework: What Garnet Compositions Reveal,” in Proceedings of the Third International Conference on Creationism, Pittsburgh, PA, July 18–23, 1994. Editor R. E. Walsh, 485–496.

Ballaran, T. B., Carpenter, M. A., and Geiger, C. A. (1999). Local Structural Heterogeneity in Garnet Solid Solutions. *Phys. Chem.Miner.* 26, 554–569. doi:10.1007/s002690050219

Barrie, C. D., Cook, N. J., and Boyle, A. P. (2010). Textural Variation in the Pyrite-Rich Ore Deposits of the Røros District, Trondheim Region, Norway: Implications for Pyrite Deformation Mechanisms. *Miner Deposita* 45, 51–68. doi:10.1007/s00126-009-0261-3

Bau, M. (1991). Rare-earth Element Mobility during Hydrothermal and Metamorphic Fluid-Rock Interaction and the Significance of the Oxidation State of Europium. *Chem. Geology.* 93, 219–230. doi:10.1016/0009–2541(91)90115–8

Baxter, E. F., Caddick, M. J., and Ague, J. J. (2013). Garnet: Common Mineral, Uncommonly Useful. *Elements* 9, 415–419. doi:10.2113/gselements.9.6.415

Baxter, E. F., and Scherer, E. E. (2013). Garnet Geochronology: Timekeeper of Tectonometamorphic Processes. *Elements* 9, 433–438. doi:10.2113/gselements.9.6.433

Bernard, J. W., Ekaterina, S. K., and Andrew, K. M. (2013). Garnet in the Earth’s Mantle. *Elements* 9 (6), 421–426. doi:10.2113/gselements.9.6.421

Burton, K. W., Bourdon, B., Birck, J.-L., Allègre, C. J., and Hein, J. R. (1999). Osmium Isotope Variations in the Oceans Recorded by FeMn Crusts. *Earth Planet. Sci. Lett.* 171, 185–197. doi:10.1016/S0012–821X(99)00139–9

Chai, F., Mao, J., Dong, L., Yang, F., Liu, F., Geng, X., et al. (2009). Geochronology of Metarhyolites from the Kangbutiebao Formation in the Kelang basin, Altay Mountains, Xinjiang: Implications for the Tectonic Evolution and Metallogeny. *Gondwana Res.* 16, 189–200. doi:10.1016/j.gr.2009.03.002

Charles, A. G. (2016). A Tale of Two Garnets: The Role of Solid Solution in the Development toward a Modern Mineralogy. *Am. Mineral.* 101, 1735–1749. doi:10.2138/am–2016–5522

Chen, Y. J., Pirajno, F., Wu, G., Qi, J. P., and Xiong, X. L. (2012). Epithermal Deposits in North Xinjiang, NW China. *Int. J. Earth Sci. (Geol Rundsch)* 101, 889–917. doi:10.1007/s00531–011–0689–4

Chen, Y. J. (2000). Progress in the Study of Central Asia-type Orogenesis-Metallogenesis in Northwest China. *Geol. J. China Univ.* 6, 17–22. (in Chinese with English abstract). doi:10.16108/j.issn1006-7493.2000.01.002

Cheng, H., Zhang, C., Vervoort, J. D., Lu, H., Wang, C., and Cao, D. (2012). Zircon U-Pb and Garnet Lu-Hf Geochronology of Eclogites from the Lhasa Block, Tibet. *Lithos* 155, 341–359. doi:10.1016/j.lithos.2012.09.011

Ciobanu, C. L., and Cook, N. J. (2004). Skarn textures and a case study: the Ocna de Fier-Dognecea orefield, Banat, Romania. *Ore Geology. Rev.* 24, 315–370. doi:10.1016/j.oregeorev.2003.04.002

Crowe, D. E., Riciputi, L. R., Bezenek, S., and Ignatiev, A. (2001). Oxygen Isotope and Trace Element Zoning in Hydrothermal Garnets: Windows into Large-Scale Fluid Flow Behavior. *Geology* 29, 479–482. doi:10.1130/0091–7613(2001)029<0479:OIATEZ>2.0.CO;2

Dietrich, R. V. (2020). Garnet Encyclopedia Britannica. Available at: https://www.britannica.com/science/garnet (Accessed March 5, 2021).

Doyle, M. G., and Allen, R. L. (2003). Subsea-floor Replacement in Volcanic-Hosted Massive Sulfide Deposits. *Ore Geology. Rev.* 23, 183–222. doi:10.1016/S0169–1368(03)00035–0

Dziggel, A., Wulff, K., Kolb, J., Meyer, F. M., and Lahaye, Y. (2009). Significance of Oscillatory and bell-shaped Growth Zoning in Hydrothermal Garnet: Evidence from the Navachab Gold deposit, Namibia. *Chem. Geology.* 262, 262–276. doi:10.1016/j.chemgeo.2009.01.027

Fernando, G. W. A. R., Hauzenberger, C. A., Baumgartner, L. P., and Hofmeister, W. (2003). Modeling of Retrograde Diffusion Zoning in Garnet: Evidence for Slow Cooling of Granulites from the Highland Complex of Sri Lanka. *Mineralogy Pet.* 78, 53–71. doi:10.1007/s00710–002–0224–1

García-Ruiz, J. M., and Otálora, F. (2015). “Crystal Growth in Geology.” in *Handbook of Crystal Growth*. Second Edition. Editor T. Nishinaga (Boston: RudolphElsevier), 1–43. doi:10.1016/B978–0–444–63303–3.00001–8

Gaspar, M., Knaack, C., Meinert, L. D., and Moretti, R. (2008). REE in Skarn Systems: a LA-ICP-MS Study of Garnets from the Crown Jewel Gold deposit. *Geochimica et Cosmochimica Acta* 72, 185–205. doi:10.1016/j.gca.2007.09.033

Gaspar, M. (2005). The Crown Jewel Gold Skarn deposit. [Ph.D. Thesis]. Washington, DC: State University.

Geiger, C. A., Winkler, B., and Langer, K. (1989). Infrared Spectra of Synthetic Almandine-Grossular and Almandine-Pyrope Garnet Solid Solutions: Evidence for Equivalent Site Behaviour. *Mineral. Mag.* 53, 231–237. doi:10.1180/minmag.1989.053.370.10

Gemmell, J. B., Zantop, H., and Meinert, L. D. (1992). Genesis of the Aguilar zinc-lead-silver deposit, Argentina; Contact Metasomatic vs. Sedimentary Exhalative. *Econ. Geol.* 87, 2085–2112. doi:10.2113/gsecongeo.87.8.2085

Gerya, T. V., Perchuk, L. L., Triboulet, C., Audren, C., and Sez’ko, A. I. (1997). Petrology of the Tumanshet Zonal Metamorphic Complex, Eastern Sayan. *Petrology* 5, 503–533 .

Goldfarb, R. J., Mao, J. W., Hart, C., Wang, D., Anderson, E., and Wang, Z. (2003). “Tectonic and Metallogenic Evolution of the Altay Shan, Northern Xinjiang Uygur Autonomous Region, Northwestern China,,” in *Tectonic Evolution and Metallogeny of the Chinese Altay and Tianshan*. Editors J. W. Mao, R. J. Goldfarb, R. Seltmann, D. H. Wang, W. J. Xiao, and C. Hart (London: Natural History Museum).

Hickmott, D., and Spear, F. S. (1992). Major-and Trace-Element Zoning in Garnets from Calcareous Pelites in the NW Shelburne Falls Quadrangle, Massachusetts: Garnet Growth Histories in Retrograded Rocks. *J. Pet.* 33, 965–1005. doi:10.1093/petrology/33.5.965

Hoal, K. E. O., Hoal, B. G., Erlank, A. J., and Shimizu, N. (1994). Metasomatism of the Mantle Lithosphere Recorded by Rare Earth Elements in Garnets. *Earth Planet. Sci. Lett.* 126, 303–313. doi:10.1016/0012–821X(94)90114–7

Holland, T., and Blundy, J. (1994). Non-ideal Interactions in Calcic Amphiboles and Their Bearing on Amphibole-Plagioclase Thermometry. *Contr. Mineral. Petrol.* 116, 433–447. doi:10.1007/BF00310910

Huang, F., He, Z., Schmidt, M. W., and Li, Q. (2014). *The Effect of* fO_2 *on Partition Coefficients of U and Th between Garnet and Silicate Melt*. America, San Francisco: Agu Fall MeetingAGU Fall Meeting Abstracts.

Jahn, B.-M. (2004). The Central Asian Orogenic Belt and Growth of the continental Crust in the Phanerozoic. *Geol. Soc. Lond. Spec. Publications* 226, 73–100. doi:10.1144/GSL.SP.2004.226.01.05

Jamtveit, B. (1991). Oscillatory Zonation Patterns in Hydrothermal Grossular-Andradite Garnet. Nonlinear Dynamics in Regions of Immiscibility. *Am. Mineral.* 76, 1319–1327 .

Jamtveit, B., and Hervig, R. L. (1994). Constraints on Transport and Kinetics in Hydrothermal Systems From Zoned Garnet Crystals. *Science* 263, 505–508. doi:10.1126/science.263.5146.505

Jamtveit, B., Wogelius, R. A., and Fraser, D. G. (1993). Zonation Patterns of Skarn Garnets: Records of Hydrothermal System Evolution. *Geology* 21, 113–116. doi:10.1130/0091–7613(1993)021<0113:ZPOSGR>2.3.CO;2

Jeremy, P. R., and Hamid, M. (2013). Magmatic-hydrothermal Processes within an Evolving Earth: Iron Oxide-Copper-Gold and Porphyry Cu ± Mo ± Au Deposits. *Geology* 41, 767–770. doi:10.1130/G34275.1

Konrad-Schmolke, M., Handy, M. R., Babist, J., and O'Brien, P. J. (2005). Thermodynamic Modelling of Diffusion-Controlled Garnet Growth. *Contrib. Mineral. Petrol.* 149, 181–195. doi:10.1007/s00410–004–0643–6

Laurent, S., Charvet, J., Shu, L. S., Ma, R. S., and Lu, H. F. (2002). Paleozoic Late Collisional Strike-Slip Deformations in Tianshan and Altay, Eastern Xinjiang, NW China. *Terra Nova* 14, 249–256. doi:10.1046/j.1365–3121.2002.00417.x

Liang, P., Zhang, Y., and Xie, Y. (2021). Chemical Composition and Genesis Implication of Garnet from the Laoshankou Fe-Cu-Au Deposit, the Northern Margin of East Junggar, NW China. *Minerals* 11, 334. doi:10.3390/min11030334

Longerich, H. P., Jackson, S. E., and Günther, D. (1996). Inter-laboratory Note. Laser Ablation Inductively Coupled Plasma Mass Spectrometric Transient Signal Data Acquisition and Analyte Concentration Calculation. *J. Anal. Spectrom.* 11, 899–904. doi:10.1039/ja9961100899

Lottermoser, B. G. (1992). Rare Earth Elements and Hydrothermal Ore Formation Processes. *Ore Geology. Rev.* 7, 25–41. doi:10.1016/0169–1368(92)90017–F

Marco, T. E., and Donald, M. B. (1982). Introduction; Terminology, Classification, and Composition of Skarn Deposits. *Econ. Geol.* 77, 745–754. doi:10.2113/gsecongeo.77.4.745

Martin, L. A. J., Ballèvre, M., Boulvais, P., Halfpenny, A., Vanderhaeghe, O., Duchêne, S., et al. (2011). Garnet Re-equilibration by Coupled Dissolution Reprecipitation: Evidence from Textural, Major Element and Oxygen Isotope Zoning of 'cloudy' Garnet. *J. Metamorph. Geol.* 29, 21–231. doi:10.1111/j.1525–1314.2010.00912.x

Meinert, L. D., Dipple, G. M., and Nicolescu, S. (2005). World Skarn Deposits. *Econ. Geol.* 100, 299–336. doi:10.5382/AV100.11

Menzer, G. (1926). Die kristallstructure von granat. *Zeitschift fu¨r Kristallographie.* 63, 157–158 .

Ottonello, G., Bokreta, M., and Sciuto, P. F. (1996). Parameterization of Energy and Interactions in Garnets; End-Member Properties. *Am. Mineral.* 81, 429–447. doi:10.2138/am–1996–3–417

Ottonello, G., and Moretti, R. (1998). On the Significance of Static Interactions in Silicate Garnets. *J. Phys. Chem. Sol.* 59, 893–901. doi:10.1016/S0022–3697(98)00030–4

Park, C., Park, C., Song, Y., and Choi, S.-G. (2019). Sequential Trace Element Analysis of Zoned Skarn Garnet: Implications for Multi-Stage Fluxing and Flow of Magmatic Fluid into a Skarn System. *Lithos* 350-351, 105213. doi:10.1016/j.lithos.2019.105213

Park, C., Song, Y., Kang, I.-M., Shim, J., Chung, D., and Park, C.-S. (2017). Metasomatic Changes during Periodic Fluid Flux Recorded in Grandite Garnet from the Weondong W-Skarn deposit, South Korea. *Chem. Geology.* 451, 135–153. doi:10.1016/j.chemgeo.2017.01.011

Pertermann, M., Hirschmann, M. M., Hametner, K., Günther, D., and Schmidt, M. W. (2004). Experimental Determination of Trace Element Partitioning between Garnet and Silica-Rich Liquid during Anhydrous Partial Melting of MORB-like Eclogite. *Geochem. Geophys. Geosyst.* 5, a–n. doi:10.1029/2003GC000638

Scherer, E. E., Cameron, K. L., and Blichert-Toft, J. (2000). Lu-Hf Garnet Geochronology: Closure Temperature Relative to the Sm-Nd System and the Effects of Trace mineral Inclusions. *Geochimica et Cosmochimica Acta* 64, 3413–3432. doi:10.1016/S0016–7037(00)00440–310.1016/s0016-7037(00)00440-3

Schmidt, A., Mezger, K., and O'Brien, P. J. (2011). The Time of Eclogite Formation in the Ultrahigh Pressure Rocks of the Sulu Terrane. *Lithos* 125, 743–756. doi:10.1016/j.lithos.2011.04.004

Shannon, R. D. (1976). Revised Effective Ionic Radii and Systematic Studies of Interatomic Distances in Halides and Chalcogenides. *Acta Cryst. Sect A.* 32, 751–767. doi:10.1107/S0567739476001551

Smith, M. P., Henderson, P., Jeffries, T. E. R., Long, J., and Williams, C. T. (2004). The Rare Earth Elements and Uranium in Garnets from the Beinn an Dubhaich Aureole, Skye, Scotland, UK: Constraints on Processes in a Dynamic Hydrothermal System. *J. Pet.* 45, 457–484. doi:10.1093/petrology/egg087

Stefanie, M. B., Stephen, J. P., Paul, J. S., Stephanie, M., and Larry, P. (2014). Evidence for Syngenetic Precious Metal Enrichment in an Appalachian Volcanogenic Massive Sulfide System: The 1806 Zone, Ming Mine, Newfoundland, Canada. *Econ. Geol.* 109, 1611–1642. doi:10.2113/econgeo.109.6.1611

Sun, S.-s., and McDonough, W. F. (1989). Chemical and Isotopic Systematics of Oceanic Basalts: Implications for Mantle Composition and Processes. *Geol. Soc.* 42, 313–345. doi:10.1144/GSL.SP.1989.042.01.19

Sverjensky, D. A. (1984). Europium Redox Equilibria in Aqueous Solution. *Earth Planet. Sci. Lett.* 67, 70–78. doi:10.1016/0012–821X(84)90039–610.1016/0012-821x(84)90039-6

Triboulet, C. (1992). The (Na?Ca)amphibole?albite?chlorite?epidote?quartz Geothermobarometer in the System S?A?F?M?C?N?H2O. 1. An Empirical Calibration. *J. Metamorph. Geol.* 10, 545–556. doi:10.1111/j.1525–1314.1992.tb00104.x

Vander, A. J., and Andre, L. (1991). Trace Elements (REE) and Isotopes (O, C, Sr) to Characterize the Metasomatic Fluid Sources: Evidence from the Skarn deposit (Fe, W, Cu) of Traversella (Ivrea, Italy). *Contrib. Miner. Petrol.* 106, 325–339. doi:10.1007/BF00324561

Wan, B., Zhang, L., and Xiang, P. (2010a). The Ashele VMS-type Cu-Zn deposit in Xinjiang, NW China Formed in a Rifted Arc Setting. *Resour. Geol.* 60, 150–164. doi:10.1111/j.1751–3928.2010.00122.x

Wan, B., Zhang, L., and Xiao, W. (2010b). Geological and Geochemical Characteristics and Ore Genesis of the Keketale VMS Pb-Zn deposit, Southern Altai Metallogenic Belt, NW China. *Ore Geology. Rev.* 37, 114–126. doi:10.1016/j.oregeorev.2010.01.002

Wang, J. B., Qin, K. Z., Wu, Z. L., Hu, J. H., and Deng, J. N. (1998). *Volcanic-exhalative-sedimentary Lead Zinc Deposit in the Southern Margin of the Altai.* XinjiangBeijing: Geology Publishing House. (in Chinese).

Wiedenbeck, M., Allé, P., Corfu, F., Griffin, W. L., Meier, M., Oberli, F., et al. (1995). Three Natural Zircon Standards for U-Th-Pb, Lu-Hf, Trace Element and REE Analyses. *Geostand. Newslett.* 19, 1–23. doi:10.1111/j.1751–908X.1995.tb00147

Xia, Q.-X., Wang, H.-Z., Zhou, L.-G., Gao, X.-Y., Zheng, Y.-F., Van Orman, J. A., et al. (2016). Growth of Metamorphic and Peritectic Garnets in Ultrahigh-Pressure Metagranite during continental Subduction and Exhumation in the Dabie Orogen. *Lithos* 266-267, 158–181. doi:10.1016/j.lithos.2016.08.043

Xiao, W. J., Windley, B. F., Huang, B. C., Han, C. M., Yuan, C., Chen, H. L., et al. (2009). End-Permian to Mid-triassic Termination of the Accretionary Processes of the Southern Altaids: Implications for the Geodynamic Evolution, Phanerozoic continental Growth, and Metallogeny of Central Asia. *Int. J. Earth Sci. (Geol Rundsch)* 98, 1189–1217. doi:10.1007/s00531–008–0407–z

Xiao, X., Zhou, T.-f., White, N. C., Zhang, L.-j., Fan, Y., Wang, F.-y., et al. (2018). The Formation and Trace Elements of Garnet in the Skarn Zone from the Xinqiao Cu-S-Fe-Au deposit, Tongling Ore District, Anhui Province, Eastern China. *Lithos* 302-303, 467–479. doi:10.1016/j.lithos.2018.01.023

Xu, J., Ciobanu, C. L., Cook, N. J., Zheng, Y., Sun, X., and Wade, B. P. (2016). Skarn Formation and Trace Elements in Garnet and Associated Minerals from Zhibula Copper deposit, Gangdese Belt, Southern Tibet. *Lithos* 262, 213–231. doi:10.1016/j.lithos.2016.07.010

Xu, J., Hart, C. J. R., Wang, L., Chu, H., Lin, L., Wei, X., et al. (2011). Carbonic Fluid Overprints in Volcanogenic Massive Sulfide Deposits: Examples from the Kelan Volcanosedimentary Basin, Altaides, China. *Econ. Geology.* 106, 145–155. doi:10.2113/econgeo.106.1.145

Xu, J. H., Shan, L. H., Ding, R. F., Craig, H., Wang, L. L., and Wei, X. F. (2008). Carbonic Fluid Inclusion Assemblages and Their Geological Significance at the Tiemurte Lead–Zinc Deposit, Altay. *Acta Petrologica Sinica.* 24, 2094–2104. (in Chinese with English abstract)

Yang, F., Geng, X., Wang, R., Zhang, Z., and Guo, X. (2018). A Synthesis of Mineralization Styles and Geodynamic Settings of the Paleozoic and Mesozoic

Metallic Ore Deposits in the Altay Mountains, NW China. *J. Asian Earth Sci.* 159, 233–258. doi:10.1016/j.jseaes.2017.05.020\

Yardley, B. W. D., Rochelle, C. A., Barnicoat, A. C., and Lloyd, G. E. (1991). Oscillatory Zoning in Metamorphic Minerals: an Indicator of Infiltration Metasomatism. *Mineral. Mag.* 55, 357–365. doi:10.1180/minmag.1991.055.380.06

Yu, P.-P., Zheng, Y., and Wang, C.-M. (2020). Trace Elemental and Sulfur-lead Isotopic Variations in Metamorphosed Volcanogenic Massive Sulfide (VMS) Mineralization Systems: An Example from the Keketale Pb-Zn(-Ag) deposit, NW China. *Ore Geology. Rev.* 125, 103685. doi:10.1016/j.oregeorev.2020.103685

Yu, P., and Zheng, Y. (2019). Pb-Zn-Cu Accumulation from Seafloor Sedimentation to Metamorphism: Constraints from Ore Textures Coupled with Elemental and Isotopic Geochemistry of the Tiemurt in Chinese Altay Orogen, NW China. *Gondwana Res.* 72, 65–82. doi:10.1016/j.gr.2019.02.007

Zang, Z. J., Dong, L. L., Liu, W., Zhao, H., Wang, X. S., Cai, K. D., et al. (2019). Garnet U-Pb and O Isotopic Determinations Reveal a Shear-Zone Induced Hydrothermal System. *Sci. Rep.* 9, 10382. doi:10.1038/s41598–019–46868–4

Zhai, D.-G., Liu, J.-J., Zhang, H.-Y., Wang, J.-P., Su, L., Yang, X.-A., et al. (2014). Origin of Oscillatory Zoned Garnets from the Xieertala Fe-Zn Skarn deposit, Northern China: *In Situ* LA-ICP-MS Evidence. *Lithos* 190-191, 279–291. doi:10.1016/j.lithos.2013.12.017

Zhang, L., Zheng, Y., and Chen, Y. (2012). Ore Geology and Fluid Inclusion Geochemistry of the Tiemurt Pb-Zn-Cu deposit, Altay, Xinjiang, China: A Case Study of Orogenic-type Pb-Zn Systems. *J. Asian Earth Sci.* 49, 69–79. doi:10.1016/j.jseaes.2011.11.019

Zhang, Y., Liu, Q., Shao, Y., and Li, H. (2017a). Fingerprinting the Hydrothermal Fluid Characteristics from LA-ICP-MS Trace Element Geochemistry of Garnet in the Yongping Cu Deposit, SE China. *Minerals* 7, 199. doi:10.3390/min7100199

Zhang, Y., Shao, Y.-J., Wu, C.-d., and Chen, H.-Y. (2017b). LA-ICP-MS Trace Element Geochemistry of Garnets: Constraints on Hydrothermal Fluid Evolution and Genesis of the Xinqiao Cu-S-Fe-Au deposit, Eastern China. *Ore Geology. Rev.* 86, 426–439. doi:10.1016/j.oregeorev.2017.03.005

Zhao, B., Zhao, J. S., and Liu, H. C. (1999). REE Geochemical Studies of Whole Rock and Rockforming Minerals in Skarns from Cu (Au), Cu-Fe (Au) and Fe Ore Deposits Distributed along Middle-Lower Reaches of Yangtze River, China. *Geochimica* 28, 113–125. (in Chinese with English abstract) .

Zheng, Y., Zhang, L., Chen, Y.-j., Hollings, P., and Chen, H.-y. (2013b). Metamorphosed Pb-Zn-(Ag) Ores of the Keketale VMS deposit, NW China: Evidence from Ore Textures, Fluid Inclusions, Geochronology and Pyrite Compositions. *Ore Geology. Rev.* 54, 167–180. doi:10.1016/j.oregeorev.2013.03.009

Zheng, Y., Zhang, L., Chen, Y.-J., Qin, Y.-J., and Liu, C.-F. (2012). Geology, Fluid Inclusion Geochemistry, and 40Ar/39Ar Geochronology of the Wulasigou Cu deposit, and Their Implications for Ore Genesis, Altay, Xinjiang, China. *Ore Geology. Rev.* 49, 128–140. doi:10.1016/j.oregeorev.2012.09.005

Zheng, Y., Zhang, L., and Guo, Z. L. (2013a). Zircon LA-ICP-MS U-Pb and Biotite 40Ar/39Ar Geochronology of the Tiemurt Pb-Zn-Cu deposit, Xinjiang: Implications for the Ore Genesis. *Acta Petrol. Sin.* 29, 191–204. (in Chinese with English abstract) .

Zheng, Y., Zhang, L., Li, D.-F., Kapsiotis, A., and Chen, Y.-J. (2015). Genesis of the Dadonggou Pb-Zn deposit in Kelan basin, Altay, NW China: Constraints from Zircon U-Pb and Biotite 40Ar/39Ar Geochronological Data. *Ore Geology. Rev.* 64, 128–139. doi:10.1016/j.oregeorev.2014.07.002

Zhou, L.-G., Xia, Q.-X., Zheng, Y.-F., and Hu, Z. (2014). Polyphase Growth of Garnet in Eclogite from the Hong'an Orogen: Constraints from Garnet Zoning and Phase Equilibrium. *Lithos* 206-207, 79–99. doi:10.2113/gselements.9.6.415

Zhuang, Y. X. (1994). *Tectonothermal Evolution in Space and Time and Orogenic Process of Altaide, China*. Changchun: Jilin Scientific and Technical Press. (in Chinese).

Conflict of Interest: The authors declare that the research was conducted in the absence of any commercial or financial relationships that could be construed as a potential conflict of interest.